ACKNOWLEDGMENT

This study was supported in part by the Grant in Aid for Scientific Research from the Ministry of the Health and Labor (to S. O.), Japan. The authors gratefully acknowledge the technical support of Miss Masami Yokoyama for her technical assistance.

REFERENCES

[1] S. Aburatani and W. Fujibuchi, "Application of Structural Equation Modeling for Inferring Toxicity-Dependent Regulation in Human Embryonic Stem Cells," GLOBAL HEALTH 2012 paper, pp.27-32, Oct. 2012.

[2] A. Baccarelli and V. Bollati, "Epigenetics and environmental chemicals," Curr. Opin. Pediatr. vol. 21(2), Apr. 2009, pp. 243-251, doi:10.1097/MOP.0b013e32832925cc.

[3] L. Hou, X. Zhang, D. Wang, and A. Baccarelli, "Environmental chemical exposures and human epigenetics," Int. J. Epidemiol., vol. 41(1), Feb. 2012, pp. 79–105, doi:10.1093/ije/dyr154.

[4] Y. Yuan, "Methylmercury: a potential environmental risk factor contributing to epileptogenesis," Neurotoxicology, vol. 33(1), Jan. 2012, pp. 119–126, doi:10.1016/j.neuro. 2011.12. 014.

[5] N. Tatsuta, et al., "Prenatal exposures to environmental chemicals and birth order as risk factors for child behavior problems," Environ. Res., vol. 114, Apr. 2012, pp. 47–52, doi: 10.1016/j.envres.2012.02.001.

[6] D. A. Rappolee, Y. Xie, J. A. Slater, S. Zhou, and E. E. Puscheck, "Toxic stress prioritizes and imbalances stem cell differentiation: implications for new biomarkers and in vitro toxicology tests," Syst. Biol. Reprod. Med., vol. 58(1), Feb. 2012, pp. 33–40, doi:10.3109/19396368.2011.647381.

[7] X. He, et al., "Effects of methylmercury exposure on neuronal differentiation of mouse and human embryonic stem cells," Toxicol. Lett., vol. 212(1), Apr. 2012, pp. 1–10, doi: 10.1016/j.toxlet.2012.04.011.

[8] J. A. Harrill, B. L. Robinette, and W. R. Mundy, "Use of high content image analysis to detect chemical-induced changes in synaptogenesis in vitro," Toxicol. In Vitro, vol. 25(1), Feb. 2011, pp. 368–387, doi:10.1016/j.tiv.2010.10.011.

[9] U. Gündel, D. Benndorf, M. von Bergen, R. Altenburger, and E. Küster, "Vitellogenin cleavage products as indicators for toxic stress in zebra fish embryos: A proteomic approach," Proteomics, vol. 7(24), Dec. 2007, pp. 4541–4554, doi: 10.1002/pmic.200700381

[10] J. Thompson and J. Bannigan, "Cadmium: toxic effects on the reproductive system and the embryo," Reprod. Toxicol., vol. 25(3), Apr. 2008, pp. 304–315, doi: 10.1016/j.reprotox.2008.02.001.

[11] T. Akutsu, S. Miyano, and S. Kuhara, "Algorithms for identifying Boolean networks and related biological networks based on matrix multiplication and fingerprint function," J. Comput. Biol., vol. 7, Aug. 2000, pp. 331-343, doi:10.1089/ 106652700750050817.

[12] N. Friedman, M. Linial, I. Nachman, and D. Pe'er, "Using Bayesian networks to analyze expression data," J. Comput. Biol., vol. 7, Jul. 2000, pp. 601–620, doi:10.1089/ 106652700750050961.

[13] S. Aburatani, S. Kuhara, H. Toh, and K. Horimoto, "Deduction of a gene regulatory relationship framework from gene expression data by the application of graphical Gaussian modeling," Signal Processing, vol. 83, Apr. 2003, pp. 777–788, doi:10.1016/S0165-1684(02)00476-0.

[14] S. Aburatani, "Development of network inference among LexA/RecA-dependent manner genes in the SOS response," J. of Nucleic Acids Investigation, vol. 1, Oct. 2010, pp. e13–e17, doi:10.4081/jnai.2010.e13.

[15] S. Aburatani, "Application of structure equation modeling for inferring a serial transcriptional regulation in yeast," Gene. Regul. Syst. Bio., vol. 5, Nov. 2011, pp. 75–88, doi:10.4137/ GRSB.S7569.

[16] S. Aburatani, "Network Inference of pal-1 Lineage-Specific Regulation in the C. elegans Embryo by Structural Equation Modeling," Bioinformation, vol. 8(14), Aug. 2011, pp. 652–657, doi:10.6026/97320630008652.

[17] K. A. Bollen, Structural Equations with Latent Variables, New York: Wiley-Interscience, 1989.

[18] O. D. Duncan, Introduction to Structural Equation Models, New York: Academic Press, 1975.

[19] J. Pearl, Causality: Models, Reasoning, and Inference, 2nd ed., Cambridge: Cambridge University Press, 2001.

[20] W. Fujibuchi, et al., "Prediction of Chemical Toxicity by Network-based SVM on ES-cell Validation System," Proc. of the 2011 Joint Conference of CBI-Society and JSBi, pp.47, Nov. 2011.

[21] J. Neter, M. Kutner, W. Wasserman, and C. Nachtsheim, Applied Linear Statistical Models, 5th ed., Chicago: Irwin, 2006.

[22] L. Li and G. E. Caldwell, "Coefficient of cross correlation and the time domain correspondence," Journal of Electromyography and Kinesiology, vol. 9, Dec. 1999, pp. 385–389, doi:10.1016/S1050-6411(99)00012-7.

[23] K. G. Joreskog and D. Sorbom, LISREL-VI: Analysis of Linear Structural Relationships By the Method of Maximum Likelihood, Redondo Beach: Doss-Haus Books, 1984.

[24] P. Spirtes, C. Glymour, and R. Scheines, Causation, Prediction, and Search, 2nd ed., Cambridge: The MIT Press, 2001.

[25] R. Agrawal, T. Imieliński, A. Swami, "Mining association rules between sets of items in large databases," Proc. of SIGMOD'93, May 1993, pp. 207–216, doi:10.1145/170035. 170072.

[26] D. C. Rice, R. Schoeny, K. Mahaffey, "Methods and rationale for derivation of a reference dose for methylmercury by the U.S. EPA," Risk analysis: an official publication of the Society for Risk Analysis, vol. 23(1), Feb. 2003, pp. 107–115, doi:10.1111/1539-6924.00294.

[27] A. L. Choi, et al., "Methylmercury Exposure and Adverse Cardiovascular Effects in Faroese Whaling Men," Environmental Health Perspectives, vol. 117(3), 2009, pp. 367–372, doi:10.1289/ehp.11608.

[28] J. M. Rosenstein, N. Mani, A. Khaibullina, and J. M. Krum, "Neurotrophic effects of vascular endothelial growth factor on organotypic cortical explants and primary cortical neurons," J. Neurosci., vol. 23(35), pp. 11036–11044, Dec. 2003.

[29] L. H. Looijenga, et al., "POU5F1 (OCT3/4) identifies cells with pluripotent potential in human germ cell tumors," Cancer Res., vol. 63(9), pp. 2244–2250, May 2003.

[30] Y. Arai, et al., "Role of Fabp7, a Downstream Gene of Pax6, in the Maintenance of Neuroepithelial Cells during Early Embryonic Development of the Rat Cortex," J. Neurosci., vol. 25(42), pp. 9752–9761, Oct. 2005.

[31] N. Ito, et al., "Pathological markers for non-genotoxic agent-associated carcinogenesis," Toxicol. Lett., Vol. 64–65, Dec. 1992, pp. 613-620, doi:10.1016/0378-4274(92)90239-G.

[32] M. J. Iatropoulos, C. X. Wang, K. E. von Keutz, and G. M. Williams, "Assessment of chronic toxicity and carcinogenicity in an accelerated cancer bioassay in rats of Nifurtimox, an antitrypanosomiasis drug," Exp. Toxicol. Pathol., vol. 57(5-6), Jul. 2006, pp. 397–404, doi:10.1016/ j.etp.2006.01.005.

[33] K. Mitsui, "The homeoprotein Nanog is required for maintenance of pluripotency in mouse epiblast and ES cells," Cell, vol. 113(5), May 2003, pp. 631–642, doi:10.1016/S0092-8674(03)00393-3.

[34] I. Chambers, et al., "Functional expression cloning of Nanog, a pluripotency sustaining factor in embryonic stem cells," Cell, vol. 113(5), May 2003, pp. 643–655, doi:10.1016/S0092 -8674(03)00392-1.

[35] H. Hamada, C. Meno, D. Watanabe, and Y. Saijoh, "Establishment of vertebrate left-right asymmetry," Nat. Rev. Genet., vol. 3(2), Feb. 2002, pp. 103–113, doi:10.1038/nrg 732.

[36] C. Grandel and N. H. Patel, "Nodal signaling is involved in left-right asymmetry in snails," Nature, vol. 457(7232), Feb. 2009, pp. 1007–1011, doi:10.1038/nature07603.

RESEARCH PAPER

Systems Biomedicine 1:3, 1–7; July/August/September 2013; © 2013 Landes Bioscience

The impact of collapsing data on microarray analysis and DILI prediction

Jean-François Pessiot,[1,*] Pui Shan Wong,[1] Toru Maruyama,[2] Ryoko Morioka,[1] Sachiyo Aburatani,[1] Michihiro Tanaka[3] and Wataru Fujibuchi[1,2,3,*]

[1]Computational Biology Research Center; Advanced Industrial Science and Technology; Tokyo, Japan; [2]Faculty of Science and Engineering; Waseda University; Tokyo, Japan; [3]Center of iPS Cell Research and Application (CiRA); Kyoto University; Kyoto, Japan

Keywords: in vivo-in vitro comparison, gene set enrichment analysis, data collapsing, drug-induced liver injury, toxicity prediction

Abbreviations: AUC, area under the curve; DILI, drug-induced liver injury; IVV, in vivo; IVT, in vitro; GSEA, gene set enrichment analysis; ROC, receiver operating characteristic; RBF, radial basis function; SVM, support vector machine

In this work, we focus on two fundamental problems of toxicogenomics using the data provided by the Japanese toxicogenomics project. First, we analyze to what extent animal studies can be replaced by in in vitro assays. We show that the probeset-level representation achieves poor agreement between in vivo and in vitro data. We present a data collapsing approach to resolve poor data agreement between in vivo and in vitro data, as measured by GSEA analysis and AUC scores. Second, we address the difficult problem of predicting DILI using available microarray data. Using a binary classification framework, our results suggest that rat in vivo data are more informative than human in vitro data to predict DILI.

Introduction

In the field of toxicology, animal studies and in vitro experiments are frequently used as surrogates for human studies even though they have shown poor agreement so far. It is still unclear how the results obtained from one animal species, such as rats, can help important biomedical research areas for humans, such as the prediction of drug-induced liver injury (DILI). This work is an attempt to address both issues, using the toxicogenomics data set provided by the Japanese toxicogenomics project.[1]

First, we analyzed to what extent animal studies can be replaced by in in vitro assays. We compared lists of differentially expressed probesets between rat in vivo and rat in vitro data, and found poor agreement between the two. This confirmed previous studies suggesting that probeset-level analysis has major limitations, and motivated us to consider higher levels of data abstractions. Thus, we present a data collapsing approach which improves the agreement between in vivo and in vitro data. We collapsed probesets and evaluated the in vivo–in vitro agreement using Gene Set Enrichment Analysis (GSEA). We also collapsed time points and evaluated the in vivo–in vitro agreement using the binary classification framework.

Second, we addressed the problem of predicting DILI using available microarray data. DILI is the primary cause for the failure of drug candidates during clinical trials, and for the withdrawal of drugs from the market. Because of the potentially dangerous adverse effects of DILI, and because of its cost for the healthcare system and the pharmaceutical industry, the study of DILI has become an important research area in drug development.[2-5] In particular, the ability to accurately predict the DILI level of a candidate drug early in its development would be highly desirable. To this end, it is necessary to pre-process and analyze the results of toxicity assessments for various drugs and various conditions.

Intuitively, we would expect that unprocessed in vitro data are too noisy for DILI prediction and would need to be collapsed in order to achieve a better signal-to-noise ratio. In contrast, we would also expect unprocessed in vivo data to contain information that is important for predicting DILI. This information could be lost during data collapsing, resulting in a lower prediction performance. Our prediction results tend to confirm these assumptions, and suggest to use unprocessed in vivo data simultaneously with collapsed in vitro data to improve the prediction performance of DILI.

Results

Comparison between in vivo and in vitro data. *Probeset-level differential expression analysis.* We studied the similarity between in vivo and in vitro data at the probeset-level using differential expression analysis. Using empirical Bayes statistics, we tested for agreement between in vivo and in vitro probesets at corresponding time points. In our experiments, we obtained AUC = 0.56 for t_{IVV} = 3 h and t_{IVT} = 2 h, AUC = 0.56 at t_{IVV} = 9 h and t_{IVT} = 8 h and AUC = 0.60 at t_{IVV} = 24 h and t_{IVT} = 24 h (**Fig. 1**).

*Correspondence to: Jean-François Pessiot and Wataru Fujibuchi; Email: jfk.pessiot@aist.go.jp and w.fujibuchi@cira.kyoto-u.ac.jp
Submitted: 10/23/12; Revised: 12/10/12; Accepted: 12/31/12
http://dx.doi.org/10.4161/sysbiomad.24255

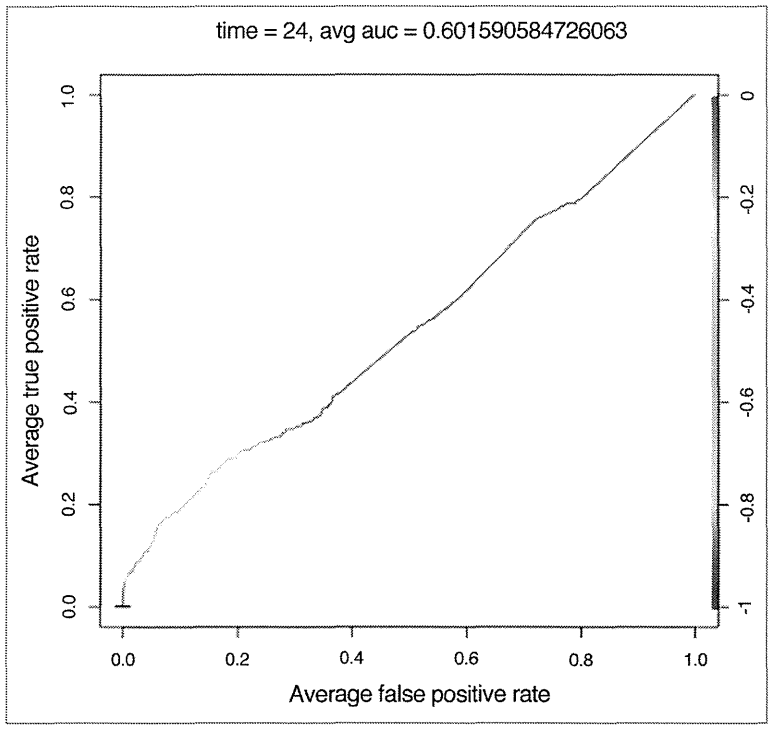

Figure 1. Comparison between in vivo and in vitro differentially expressed probesets at t_{IVV} = 24 h and t_{IVT} = 24 h.

Gene set enrichment analysis procedure. Data overlap between IVT and IVV. In our initial GSEA analyses, we assessed whether expression patterns between the two data sets were significantly similar by comparing in vivo and in vitro data at two time points for each of the 131 drugs in both directions. For each drug, there were four possible outcomes: all four analyses were significantly enriched ($p < 0.05$), meaning there was full agreement with expression patterns between in vivo and in vitro data; three analyses were significantly enriched, meaning there was full agreement with expression patterns at one time point but not the other; two analyses were significantly enriched, meaning either there was full agreement at only one time point or there was only agreement in one direction at each time point; and one analysis was significantly enriched, meaning the expression pattern did not agree except at one time point in a particular direction. Of the 131 drugs analyzed, 55% were significantly enriched in all four tests, 34% were enriched in three tests, 10% were enriched in two tests and 2% were enriched for 1 test.

To check that the lists were not simply correlated, Spearman's rank correlation was calculated between each pair of in vivo and in vitro lists. The correlation coefficients were all under 0.25, indicating that there is little correlation between the lists of fold changes between in vivo and in vitro data.

Data overlap between IVT and liver function, and IVV and liver function. For the GSEA analyses against liver gene ontologies, in vivo and in vitro data were compared with predefined lists of liver gene ontologies at two time points for each of the 131 drugs. To assess whether enrichment analyses against gene ontologies were similar between in vivo and in vitro data, results were compared between in vivo data at 2 h and in vitro data at 3 h, and in vivo and in vitro data at 24 h. For each drug, there were two possible outcomes: enrichment significance was the same between in vivo and in vitro at the two time points; enrichment significance was the same at only one of the two time points; and enrichment significant was different across the two time points. Of the 131 drugs analyzed, 50% had the same enrichment results between in vivo and in vitro at the two time points, 42% had the same enrichment results at one of the time points and 8% did not share the same enrichment results at the two time points. This suggests that liver related genes are highly overexpressed or under expressed in response to 50% of the drugs in both in vivo and in vitro conditions.

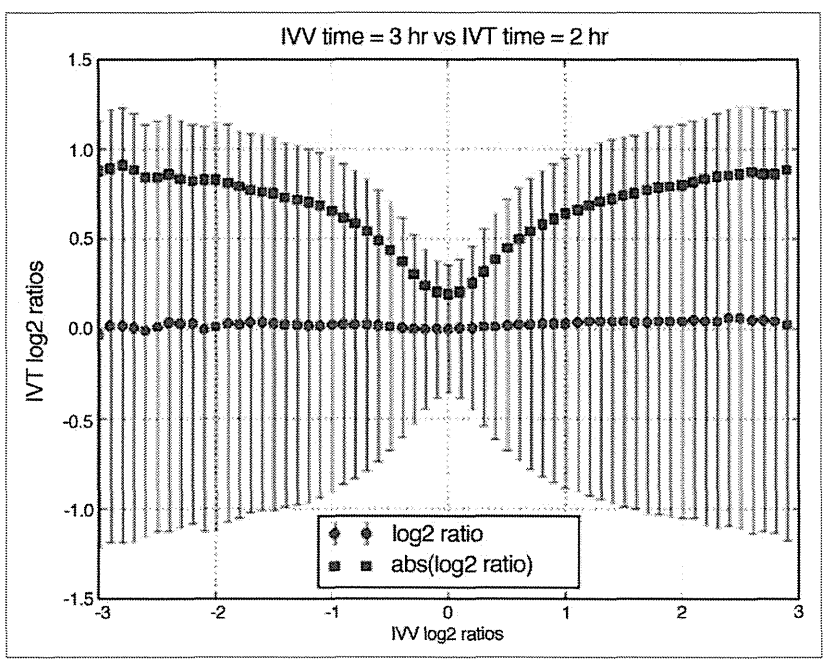

Figure 2. In vivo fold changes at t = 3 h vs. in vitro fold changes at t = 2 h.

Comparison between in vivo fold changes and in vitro fold changes. We analyzed the relationships between in vivo fold changes and in vitro fold changes. We plotted the in vitro fold change (averaged over all drugs and all doses) as a function of the in vivo fold change, at t_{IVV} = 3 h and t_{IVT} = 2 h (**Fig. 2**), and at t_{IVV} = 24 h and t_{IVT} = 24 h (**Fig. 3**).

Collapsing strategies for probesets and time points. In order to improve the signal-to-noise

ratio of the data, we considered a data collapsing approach. **Table 1** shows the various collapsing strategies and their corresponding AUC scores. The highest score AUC = 0.85 ± 0.04 was achieved when using gene-level representation, absolute fold changes, and average values over time points.

In **Figure 4**, we show the ROC curves for three data collapsing strategies. All three approaches use absolute values. The blue curve corresponds to the probeset level and time series integral strategy (AUC = 0.79). The green curve corresponds to the gene level and time series integral strategy (AUC = 0.84). The red curve corresponds to the optimal strategy: gene level, time series average (AUC = 0.85).

Correlation matrix analysis. We used the correlation matrix distances to assess the agreement between in vivo and in vitro gene expression data. **Table 2** shows the top ten genes which show the most similar behaviors between in vivo and in vitro conditions.

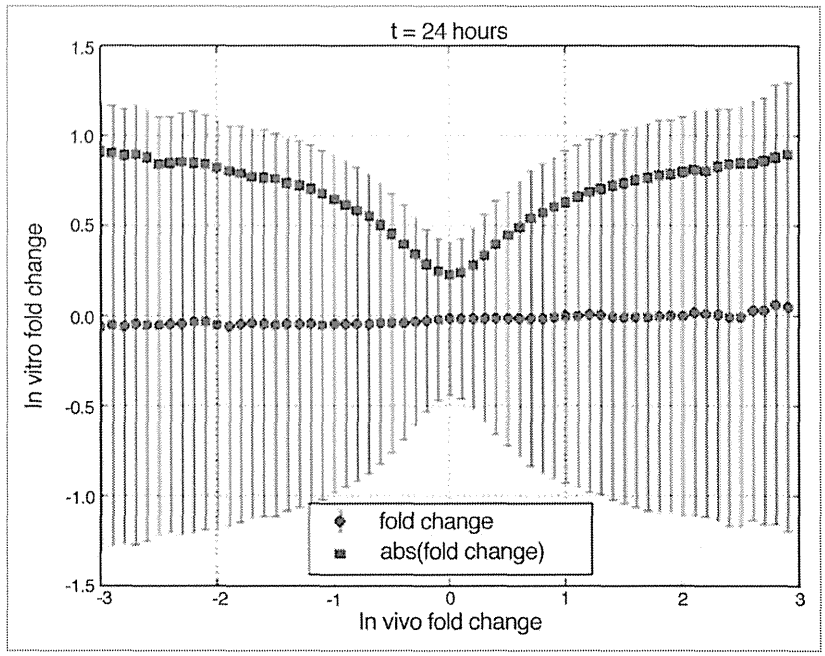

Figure 3. In vivo fold changes at t = 24 h vs. in vitro fold changes at t = 24 h.

Predicting drug-induced liver injury in humans. We considered the DILI prediction problem as a binary classification of "Most DILI" against "Less DILI or no DILI." We used two support vector machine classifiers and evaluated their classification performance using a 10-fold cross validation. **Tables 3 and 4** show the AUC scores of the linear SVM and the RBF kernel SVM, respectively.

Table 1. Data collapsing strategies and their AUC scores

Collapse probesets	Collapse time points	Collapsing strategy	Absolute values	Average AUC
False	False	First	False	0.51 ± 0.04
False	False	Last	False	0.51 ± 0.04
False	True	Integral	False	0.52 ± 0.05
False	True	Average	False	0.52 ± 0.04
True	False	First	False	0.52 ± 0.05
True	False	Last	False	0.51 ± 0.06
True	True	Integral	False	0.52 ± 0.06
True	True	Average	False	0.53 ± 0.06
False	False	First	True	0.72 ± 0.02
False	False	Last	True	0.71 ± 0.04
False	True	Integral	True	0.79 ± 0.03
False	True	Average	True	0.81 ± 0.03
True	False	First	True	0.77 ± 0.03
True	False	Last	True	0.74 ± 0.05
True	True	Integral	True	0.84 ± 0.04
True	True	Average	True	**0.85 ± 0.04**

Discussion

Comparison between in vivo and in vitro data. *Probeset-level differential expression analysis.* The results show that predicting differentially expressed probesets in vivo using in vitro experiments is a difficult task. We have AUC = 0.56 for the first two pairs of time points (t_{IVV} = 3 h and t_{IVT} = 2 h, and t_{IVV} = 9 h and t_{IVT} = 8 h), which is close to random prediction (AUC = 0.5). There is only a slight improvement at t_{IVV} = 24 h and t_{IVT} = 24 h, with AUC = 0.60.

Overall, the empirical Bayes statistics shows that the agreement between in vivo and in vitro is poor, at the probeset-level, with respect to differential expression analysis. This can be explained by the discrepancy between its expressions in the in vivo and in vitro conditions for each biological process. This can also be caused by the limitations of a probeset-level analysis. Therefore, we need to consider higher levels of data abstractions, and compare the in vivo and in vitro data at the gene level.

Gene set enrichment analysis procedure. Although the original GSEA concept used signed fold change values, we decided to perform GSEA on absolute fold changes due to the observations in **Figures 2 and 3**. Our GSEA results show that most highly expressed or under expressed probe expression in vitro respond to drugs similarly in an equivalent in vivo experiment and vice versa. Even though we didn't find universal agreement among all time points or direction of enrichment, more than half of the drugs caused the same probes to show extremes of expression values. This may be due to the different number of samples between the in vivo and in vitro data sets, leading to some tests being enriched in one direction but not the other. If the analyses only involved interest in highly over or under expressed genes, in vitro data can be an adequate model for in vivo data for rats. We also showed that in gene ontology enrichment analyses, in vitro data only gives the same results as in vivo half the time but that the confidence of the results may be dependent on the time point.

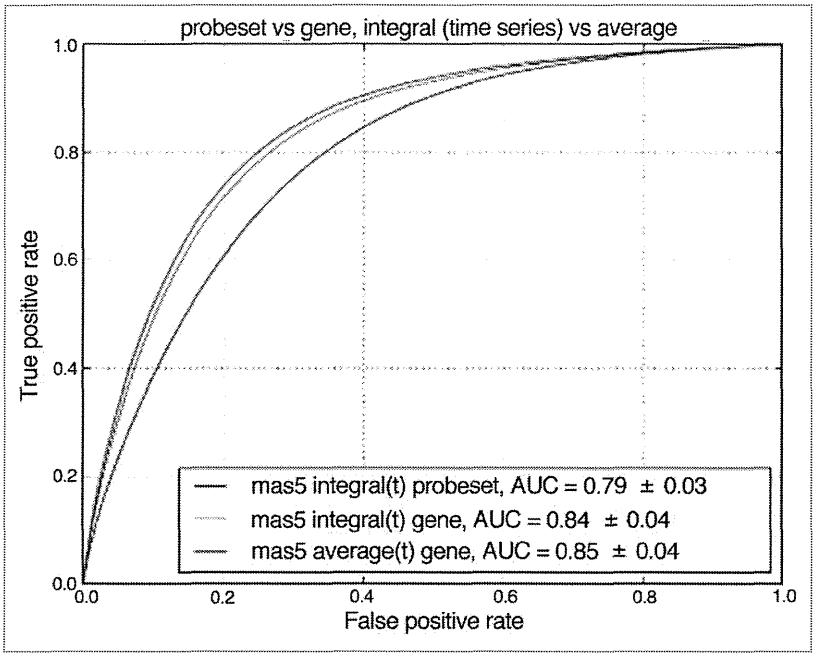

Figure 4. ROC curves for three data collapsing strategies: probeset level + time series integral (blue), gene level + time series integral (green) and gene level + time series average (red).

Table 2. Genes which behave similarly in vivo and in vitro, and their corresponding distance measures

Gene symbol	In vivo–in vitro distance	Gene Symbol	In vivo–in vitro distance
Dazap2	0.4884	Actr2	0.5808
Arf1	0.5446	Gdi2	0.5854
Aamp	0.5573	Cmpk1	0.6030
Ube2l3	0.5608	Morf4l1	0.6121
Cdc42	0.5629	Arpc2	0.6284

Comparison between in vivo fold changes and in vitro fold changes. **Figures 2 and 3** show the in vitro fold change (averaged over all drugs and all doses) as a function of the in vivo fold change. These plots show that while there is no obvious sign correlation between in vivo and in vitro data, there is a correlation between their absolute values. In other words, even if a gene has a highly positive fold change in vivo, we cannot always expect a highly positive fold change in vitro. However, a gene with a high in vivo absolute fold change tends to have a high in vitro absolute fold change as well.

To discern a biological reason behind our observations, we divided genes into two groups: genes that are congruent at signed values and genes that congruent at absolute values. More specifically, for each gene, we computed two correlation coefficients. The first one measured the correlation between the gene's fold changes in vivo and in vitro, while the second one measured the correlation between their absolute values. After filtering significant correlations ($p < 0.05$), we created two groups of genes. The first group contained genes with correlation coefficients of identical signs, while the second group contained genes with correlation coefficients of opposite signs. Then, we compared the gene ontologies for these two groups of genes. However, we did not find any distinguishable trend between the two sets of genes using gene ontology. Our observations may be due to experimental variance or further biological variance which we could not detect.

Collapsing strategies for probesets and time points. In order to improve the signal-to-noise ratio of the data, we also considered various data collapsing strategies. **Table 1** shows the details of these strategies. "Collapse probesets" is set to "True" when probesets values are averaged to their corresponding genes values, "False" otherwise. "Collapse time points" is set to "True" when each time series is collapsed to a single value. In that case, "Collapsing strategy" specifies different time collapsing strategies. With "Integral," we compute the signed integral of the time series. With "Average," we compute the average value of the time series. "Collapse time points" is set to "False" when each time series is reduced to a single time point (i.e., all other time points are discarded). In that case, "Collapsing strategy" specifies which time point of the time series is considered: the first or the last time point. "Absolute values" is set to "True" when we consider absolute fold change values, "False" when we consider the signed values.

For all strategies using signed fold change values, the corresponding AUC scores fall between 0.51 and 0.53. This confirms what we observed in **Figures 2 and 3**: the sign of a gene's fold change in vitro cannot be used to predict its sign in vivo. Thus, our following strategies use the absolute fold changes only. When we collapse probesets into genes (from 0.72 to 0.77) and time series into single values (from 0.72 to 0.79), the AUC scores improve. This is expected, as averaging helps removing the measurement noise and leads to better signal to noise ratios.

As we explained earlier, probeset-level fold changes were collapsed into gene-level fold changes by taking the average value. Another possible strategy consists in considering the maximum value instead, as noise in gene expression measurements tend to occur in probesets with low expression values. However, our experiments show no improvements with respect to AUC scores. For example, we considered the best two strategies in **Table 1**, which achieve AUC scores of 0.84 and 0.85 when considering the average fold change values. When considering the maximum values instead, the same strategies achieve 0.83 and 0.84, respectively. Therefore, when collapsing probesets into genes, we chose to focus on average values.

Surprisingly, we also observe that when collapsing a time series into a single value, computing a simple average value is slighty better than computing the integrals (AUC = 0.81 and 0.85 for the average, AUC = 0.79 and 0.84 for the integral). This result suggests that the time information is also useless, and that we can assume time independence when comparing in vivo and in

Table 3. Average AUC scores of the linear SVM for the DILI prediction problem

Collapse probesets	Collapse time points	Absolute values	Human in vitro	Rat in vitro	Rat in vivo repeated dose	Rat in vivo single dose
False	False	False	0.52 ± 0.17	0.52 ± 0.14	**0.66** ± 0.14	0.61 ± 0.12
False	True	False	0.52 ± 0.13	0.54 ± 0.15	0.56 ± 0.11	0.58 ± 0.17
True	False	False	0.50 ± 0.21	0.47 ± 0.18	0.64 ± 0.13	0.56 ± 0.20
True	True	False	0.49 ± 0.14	0.54 ± 0.13	0.58 ± 0.12	0.50 ± 0.16
False	False	True	**0.59** ± 0.08	**0.58** ± 0.08	0.61 ± 0.17	**0.67** ± 0.15
False	True	True	0.58 ± 0.12	0.55 ± 0.20	0.52 ± 0.19	0.55 ± 0.10
True	False	True	0.56 ± 0.07	0.50 ± 0.16	0.55 ± 0.18	0.62 ± 0.18
True	True	True	**0.59** ± 0.10	0.49 ± 0.12	0.59 ± 0.15	0.63 ± 0.17

Table 4. Average AUC scores of the Gaussian SVM for the DILI prediction problem

Collapse probesets	Collapse time points	Absolute values	Human in vitro	Rat in vitro	Rat in vivo repeated dose	Rat in vivo single dose
False	False	False	0.49 ± 0.19	0.51 ± 0.21	**0.65** ± 0.11	0.61 ± 0.14
False	True	False	0.49 ± 0.10	**0.58** ± 0.12	0.58 ± 0.10	0.63 ± 0.23
True	False	False	0.46 ± 0.14	0.45 ± 0.11	**0.65** ± 0.14	0.58 ± 0.13
True	True	False	0.50 ± 0.23	0.55 ± 0.19	0.61 ± 0.13	0.52 ± 0.17
False	False	True	0.59 ± 0.17	0.50 ± 0.09	0.63 ± 0.15	**0.66** ± 0.11
False	True	True	0.60 ± 0.20	0.55 ± 0.18	0.56 ± 0.21	0.51 ± 0.13
True	False	True	**0.61** ± 0.21	0.47 ± 0.15	0.59 ± 0.16	0.64 ± 0.14
True	True	True	0.60 ± 0.18	0.49 ± 0.14	0.62 ± 0.13	0.59 ± 0.13

vitro data. Overall, the best strategy uses gene-level representation, absolute fold changes, and average values over time points. The corresponding AUC score is 0.85 ± 0.04.

Predicting drug-induced liver injury in humans. Table 3 shows the classification performance of the linear SVM for different data collapsing strategies and different data sets. Overall, AUC scores tend to be low, which shows that predicting DILI using expression data are a difficult problem. We notice that the rat in vivo repeated dose and rat in vivo single dose data reach high AUC scores when no data collapsing is applied ($0.61 \leq AUC \leq 0.67$). However, collapsing either the probesets or the time points tend to decrease the AUC scores. This suggests that in vivo data might contain important information related to DILI prediction that is partially lost during data collapsing.

In contrast, the human in vitro data achieves its lowest AUC score when no pre-processing is applied (AUC = 0.52). Collapsing either the probesets or the time points tends to increase the AUC scores, although not as high as with the rat in vivo data. This suggests that even though the goal is to predict human DILI, using in vivo data from rats is more informative than using in vitro data from humans. In contrast, the rat in vitro data achieves the lowest AUC scores. This is not surprising as it combines the two limitations of the three other data sources: it is not human, and it is not in vivo.

Table 4 shows the AUC scores of the RBF kernel SVM. We observe that the highest AUC scores are achieved with the in vivo data, which confirms our similar observation with the linear SVM. But overall, the classification performance is not better than that of the linear SVM. The highest score of the kernel SVM is AUC = 0.66, compared with 0.67 for the linear SVM. This is caused by an overfitting problem: when dealing with high dimensional problems (on our case, few hundreds samples vs. tens of thousands of features), additional model complexity is not desirable.[6] These results suggest that improvements in prediction performance can be achieved by using appropriate gene filtering strategies,[7] and by combining unprocessed rat in vivo data with processed (collapsed) human in vitro data.

Materials and Methods

Data set description. We used the data set provided by the Japanese toxicogenomics project.[1] Using Affymetrix arrays, the effects of 131 drugs on the liver have been measured both in vivo (using rats) and in vitro (using human and rat hepatocytes). Among them, 101 drugs were assigned into one of the following categories, according to their FDA-approved drug labels: Most DILI concern, less DILI concern, or no DILI concern. Each drug has been tested in various conditions (time points and drug dosages), and the whole data set contains approximately 20,000 arrays. The raw CEL files have been processed using MAS5.[8-10] For the comparison between in vivo and in vitro data, three drugs (adapin, carbon tetrachloride, and chlorpromazine) were ignored because of missing values.

Statistical testing analysis. We applied empirical Bayes statistics (http://bioinf.wehi.edu.au/limma/) to test for agreement between in vivo and in vitro probesets at corresponding time points. In the in vivo data set, we identified which probesets were differentially expressed. In the in vitro data set, we computed the p values obtained from statistical testing. If the in vitro experiments were representative of the in vivo measurements, then these

in vitro p values would be low when the corresponding probesets are differentially expressed in vivo, and high otherwise.[11,12] This is a binary classification problem, and therefore, the agreement between in vivo and in vitro data can be measured by the AUC score. If AUC = 1, then the in vitro data can be used to predict which probesets are differentially expressed in vivo. If AUC = 0.5, then in vitro experiments are useless to predict them.

Gene set enrichment analysis procedure. *Data overlap between IVT and IVV.* As part of our data exploration, GSEA was used to compare the overlap between in vitro and in vivo expression data, and confirm that unsigned expression patterns between them are significantly similar. GSEA was initially used to enrich sets of expression data with biological functions[13] by comparing a ranked list from the expression data with a predefined list associated with the function of interest. During the analysis, GSEA compares the location of the elements in the predefined list with those in the ranked list, calculating the statistical significance of the total representation of the predefined list within the ranked list. The test statistic calculated determines whether the predefined list is enriched within the ranked list or not. The GSEA script used here was downloaded from the Broad Institute (www.broadinstitute.org/gsea). Related geneset-level based approaches include.[14,15]

The analyses compared in vitro and in vivo using absolute ranked lists of probe fold change values (i.e., $\log_2$ ratio). To keep the run time of the analyses reasonably low, only the top 1% of the lists were used as predefined lists. As a result the predefined lists are approximately 200–300 probes in length. The predefined lists were then enriched against the full list of the opposite experimental condition. As the goal of this data exploration was to see similarities between expression patterns, expression data was used regardless if they were significantly differentiated or not. Thus, an example enrichment analysis consisted of a predefined list of the top 1% absolute fold change in vitro data at time 2 h between control and acarbose, and a ranked list of all absolute fold change in vivo data at time 3 h between control and acarbose. GSEA was performed at two time points, 2 h for in vitro and the equivalent 3 h for in vivo, and 24 h for both in vitro and in vivo; and in both directions, in vitro data as the predefined list and in vivo data as the ranked list and vice versa. In total, four GSEA analyses were performed for each of the 131 drugs.

The expression data was normalized using MAS5 in the limma package[16] in R 2.15.1.[17] Due to the low number of replicates, fold change was calculated by combining control and low dosage into condition one, and medium and high dosage into condition two. The lists detailed above were created from the MAS5 output as described and used in the GSEA script. The output is an enrichment score and the associated p value. A p value less than 0.05 indicates that the top 1% fold change probes are expressed similarly, as a set, between in vivo and in vitro data.

Data overlap between IVT and liver function, and IVV and liver function. Following the original usage of GSEA, we also enriched the expression data against a biological function; following the main theme of the study, several liver functions were selected using gene ontology. Our goal was to see if enrichment analyses against gene ontologies would yield the same results in in vivo and in vitro data. AmiGO[18] was used to select 32 gene ontologies associated with liver which was represented by at least one probe in the data set. The 180 probes were ranked by the total number of child nodes their gene ontology had. The resulting list started with the probes of gene ontologies that had no child nodes and ended with the probes of gene ontologies with the most child nodes. These predefined gene ontology lists were then enriched against the full ranked lists in place of the top 1% lists used previously. As per the previous analyses, four GSEA analyses were performed for each of the 131 drugs.

Fold change analysis. From the raw CEL files, we extracted the MAS5 probeset-level values using LIMMA. Then, we averaged those values over biological replicates. We computed the fold changes for each condition (drug, dose and time point), i.e., the $\log_2$ ratios between the sample values and the corresponding control values.

Data collapsing strategies. We collapsed probesets into genes, by computing the average intensity of the probesets in each gene. We also collapsed each time series by computing their average absolute fold change. To evaluate our data collapsing strategy, we considered a binary classification problem where the top 1% genes with the highest in vivo average fold change were defined as true positives, and the remaining genes were defined as the true negatives. The corresponding average in vitro fold changes were used as prediction scores. When the collapsing strategy involved absolute values, we considered the average absolute fold changes instead of the signed values. The classification performance, which reflects the agreement between in vivo and in vitro data, was measured by the AUC. If AUC = 1, then the in vitro experiments can be used to predict high in vivo fold changes. If AUC = 0.5, then the in vitro experiments are useless to predict them.

Correlation matrix analysis. For a given gene, one way to assess the agreement between its in vivo and in vitro expression levels is to define a distance function between the two sets of measurements. We used the correlation matrix distance.[19-21] For each gene, we defined two correlation matrices characterizing the gene's responses to drugs in vivo and in vitro. If the Frobenius norm of the difference between these two correlation matrices is small, then the corresponding gene behaves similarly in vivo and in vitro. When running downstream analysis of in vitro data, this approach can be used to filter out inconsistent genes, and keep the genes that show high correlation between in vivo and in vitro data.

Predicting drug-induced liver injury in humans. We considered the DILI prediction problem as a binary classification of "Most DILI" against "Less DILI or no DILI." For each available data source, we considered all DILI-annotated drugs and doses with no missing data. The resulting human in vitro, rat in vitro, rat in vivo repeated dose, and rat in vivo single dose data contained 223, 303, 303, and 301 samples, respectively. Each sample corresponds to a (drug, dose) pair. The probeset space contained 54,675 probesets for humans and 31,099 probesets for rats. The gene space contained 20,026 genes for humans and 13,878 genes for rats. We used the linear SVM classifier and RBF kernel SVM classifier,[22] and evaluated their classification performance using a 10-fold cross validation. In the case of the RBF kernel, we trained a hard-margin SVM[23] (i.e., $C = +\infty$).

Disclosure of Potential Conflicts of Interest

No potential conflicts of interest were disclosed.

Acknowledgments

This work is supported by the Funding Program for World-Leading Innovative R&D on Science and Technology (FIRST program), initiated by the Council for Science and Technology Policy (CSTP). See www.tkl.iis.u-tokyo.ac.jp/FIRST/.

References

1. Uehara T, Ono A, Maruyama T, Kato I, Yamada H, Ohno Y, et al. The Japanese toxicogenomics project: application of toxicogenomics. Mol Nutr Food Res 2010; 54:218-27; PMID:20041446; http://dx.doi.org/10.1002/mnfr.200900169
2. Chen M, Vijay V, Shi Q, Liu Z, Fang H, Tong W. FDA-approved drug labeling for the study of drug-induced liver injury. Drug Discov Today 2011; 16:697-703; PMID:21624500; http://dx.doi.org/10.1016/j.drudis.2011.05.007
3. Mulrane L, Rexhepaj E, Smart V, Callanan JJ, Orhan D, Eldem T, et al. Creation of a digital slide and tissue microarray resource from a multi-institutional predictive toxicology study in the rat: an initial report from the PredTox group. Exp Toxicol Pathol 2008; 60:235-45; PMID:18479893; http://dx.doi.org/10.1016/j.etp.2007.12.004
4. McBurney RN, Hines WM, Von Tungeln LS, Schnackenberg LK, Beger RD, Moland CL, et al. The liver toxicity biomarker study: phase I design and preliminary results. Toxicol Pathol 2009; 37:52-64; PMID:19171931; http://dx.doi.org/10.1177/0192623308329287
5. Kiyosawa N, Manabe S, Sanbuissho A, Yamoto T. Gene set-level network analysis using a toxicogenomics database. Genomics 2010; 96:39-49; PMID:20363313; http://dx.doi.org/10.1016/j.ygeno.2010.03.014
6. Vapnik V. *The nature of statistical learning theory*. Springer-Verlag New York, Inc., New York, NY USA 1995
7. Lazar C, Taminau J, Meganck S, Steenhoff D, Coletta A, Molter C, et al. A survey on filter techniques for feature selection in gene expression microarray analysis. IEEE/ACM Trans Comput Biol Bioinform 2012; 9:1106-19; PMID:22350210; http://dx.doi.org/10.1109/TCBB.2012.33
8. Hubbell E, Liu WM, Mei R. Robust estimators for expression analysis. Bioinformatics 2002; 18:1585-92; PMID:12490442; http://dx.doi.org/10.1093/bioinformatics/18.12.1585
9. Pepper SD, Saunders EK, Edwards LE, Wilson CL, Miller CJ. The utility of mas5 expression summary and detection call algorithms. BMC Bioinformatics 2007; 8:273; PMID: 17663764; http://dx.doi.org/10.1186/1471-2105-8-273
10. Irizarry R. From cel files to annotated lists of interesting genes. In Gentleman R, Carey VJ, Huber W, Irizarry RA, and Dudoit S, editors, Bioinformatics and Computational Biology Solutions Using R and Bioconductor, Statistics for Biology and Health, pages 431–442. Springer New York, 2005
11. Jeffery IB, Higgins DG, Culhane AC. Comparison and evaluation of methods for generating differentially expressed gene lists from microarray data. BMC Bioinformatics 2006; 7:359; PMID:16872483; http://dx.doi.org/10.1186/1471-2105-7-359
12. Tusher VG, Tibshirani R, Chu G. Significance analysis of microarrays applied to the ionizing radiation response. Proc Natl Acad Sci U S A 2001; 98:5116-21; PMID:11309499; http://dx.doi.org/10.1073/pnas.091062498
13. Subramanian A, Tamayo P, Mootha VK, Mukherjee S, Ebert BL, Gillette MA, et al. Gene set enrichment analysis: a knowledge-based approach for interpreting genome-wide expression profiles. Proc Natl Acad Sci U S A 2005; 102:15545-50; PMID:16199517; http://dx.doi.org/10.1073/pnas.0506580102
14. Efron B, Tibshirani R. On testing the significance of sets of genes. Ann Appl Stat 2007; 1:107-29; http://dx.doi.org/10.1214/07-AOAS101
15. Jiang Z, Gentleman R. Extensions to gene set enrichment. Bioinformatics 2007; 23:306-13; PMID:17127676; http://dx.doi.org/10.1093/bioinformatics/btl599
16. Smyth GK. Limma: linear models for microarray data, pages 397–420. Springer, New York, 2005
17. R Core Team. R: A Language and Environment for Statistical Computing. R Foundation for Statistical Computing, Vienna, Austria, 2012. ISBN 3-900051-07-0
18. Ashburner M, Ball CA, Blake JA, Botstein D, Butler H, Cherry JM, et al.; The Gene Ontology Consortium. Gene ontology: tool for the unification of biology. Nat Genet 2000; 25:25-9; PMID:10802651; http://dx.doi.org/10.1038/75556
19. Luis A. Degree of polarization for three-dimensional fields as a distance between correlation matrices. Opt Commun 2005; 253:10-4; http://dx.doi.org/10.1016/j.optcom.2005.04.046
20. Luis A. Degree of coherence for vectorial electromagnetic fields as the distance between correlation matrices. J Opt Soc Am A Opt Image Sci Vis 2007; 24:1063-8; PMID:17361292; http://dx.doi.org/10.1364/JOSAA.24.001063
21. Herdin M, Czink N, Özcelik H, Bonek E. Correlation matrix distance, a meaningful measure for evaluation of non-stationary mimo channels. In Vehicular Technology Conference, pages 136–140, 2005
22. Golub TR, Slonim DK, Tamayo P, Huard C, Gaasenbeek M, Mesirov JP, et al. Molecular classification of cancer: class discovery and class prediction by gene expression monitoring. Science 1999; 286:531-7; PMID:10521349; http://dx.doi.org/10.1126/science.286.5439.531
23. Mordelet F, Vert JP. Sirene. Bioinformatics 2008; 24:76-82; http://dx.doi.org/10.1093/bioinformatics/btn273

OPEN ACCESS Freely available online

PLOS | ONE

Commensal Microbiota Contributes to Chronic Endocarditis in *TAX1BP1* Deficient Mice

Satoko Nakano[1,2], Emi Ikebe[1], Yoshiyuki Tsukamoto[3], Yan Wang[4], Takashi Matsumoto[1], Takahiro Mitsui[1], Takaaki Yahiro[1], Kunimitsu Inoue[1], Hiroaki Kawazato[5], Aiko Yasuda[5], Kanako Ito[6], Shigeo Yokoyama[7], Naohiko Takahashi[8], Mitsuo Hori[9], Tatsuo Shimada[10], Masatsugu Moriyama[3], Toshiaki Kubota[2], Katsushige Ono[4], Wataru Fujibuchi[11], Kuan-Teh Jeang[12], Hidekatsu Iha[1]*, Akira Nishizono[1]

1 Department of Microbiology, Faculty of Medicine, Oita University, Yufu, Oita, Japan, **2** Department of Ophthalmology, Faculty of Medicine, Oita University, Yufu, Oita, Japan, **3** Department of Molecular Pathology, Faculty of Medicine, Oita University, Yufu, Oita, Japan, **4** Department of Pathophysiology, Faculty of Medicine, Oita University, Yufu, Oita, Japan, **5** Research Promotion Institute, Faculty of Medicine, Oita University, Yufu, Oita, Japan, **6** Department of Internal Medicine II, Faculty of Medicine, Oita University, Yufu, Oita, Japan, **7** Department of Diagnostic Pathology, Faculty of Medicine, Oita University, Yufu, Oita, Japan, **8** Department of Laboratory Examination and Diagnostics, Faculty of Medicine, Oita University, Yufu, Oita, Japan, **9** Division of Hematology, Ibaragi Prefectural Central Hospital, Kasama, Ibaragi, Japan, **10** Department of Health Science, Oita University School of Nursing, Yufu, Oita, Japan, **11** Department of Cell Growth and Differentiation, Center for iPS Cell Research and Application, Kyoto University, Kyoto, Japan, **12** Laboratory of Molecular Microbiology, National Institute of Allergy and Infectious Diseases, National Institutes of Health, Bethesda, Maryland, United States of America

Abstract

Tax1-binding protein 1 (Tax1bp1) negatively regulates NF-κB by editing the ubiquitylation of target molecules by its catalytic partner A20. Genetically engineered *TAX1BP1*-deficient (KO) mice develop age-dependent inflammatory constitutions in multiple organs manifested as valvulitis or dermatitis and succumb to premature death. Laser capture dissection and gene expression microarray analysis on the mitral valves of *TAX1BP1*-KO mice (8 and 16 week old) revealed 588 gene transcription alterations from the wild type. *SAA3* (serum amyloid A3), *CHI3L1*, *HP*, *IL1B* and *SPP1/OPN* were induced 1,180-, 361-, 187-, 122- and 101-fold respectively. *WIF1* (Wnt inhibitory factor 1) exhibited 11-fold reduction. Intense Saa3 staining and significant I-κBα reduction were reconfirmed and massive infiltration of inflammatory lymphocytes and edema formation were seen in the area. Antibiotics-induced 'germ free' status or the additional *MyD88* deficiency significantly ameliorated *TAX1BP1*-KO mice's inflammatory lesions. These pathological conditions, as we named 'pseudo-infective endocarditis' were boosted by the commensal microbiota who are usually harmless by their nature. This experimental outcome raises a novel mechanistic linkage between endothelial inflammation caused by the ubiquitin remodeling immune regulators and fatal cardiac dysfunction.

Citation: Nakano S, Ikebe E, Tsukamoto Y, Wang Y, Matsumoto T, et al. (2013) Commensal Microbiota Contributes to Chronic Endocarditis in *TAX1BP1* Deficient Mice. PLoS ONE 8(9): e73205. doi:10.1371/journal.pone.0073205

Editor: Dong-Yan Jin, University of Hong Kong, Hong Kong

Received May 10, 2013; **Accepted** July 17, 2013; **Published** September 27, 2013

Funding: This study is supported in part by grants from the Ministry of Education, Culture, Sports, Science, and Technology; Okinawa Science and Technology Promotion Center (OSTPC); Miyazaki Prefectural Industrial Support Foundation. E.I. is a research fellow of the OSTPC and was a recipient of the Hita Tenryosui Research Scholarship from Hita Tenryosui Co. Ltd. The funders had no role in study design, data collection and analysis, decision to publish, or preparation of the manuscript.

Competing Interests: The authors have read the journal's policy and have the following conflicts: E.I. is a research fellow of the Okinawa Science and Technology Promotion Center and was a recipient of the Hita Tenryosui Research Scholarship from Hita Tenryosui Co. Ltd. There are no patents, products in development or marketed products to declare. This does not alter the authors' adherence to all the PLOS ONE policies on sharing data and materials.

* E-mail: hiha@oita-u.ac.jp

Introduction

The transcription factor NF-κB is essential for the regulation of the innate and adaptive immune responses. NF-κB is activated in response to a wide variety of stimuli, such as inflammation, DNA damage, or nociception [1,2], and is involved in embryogenesis and multiple tissue development [3]. The NF-κB family comprises five proteins including RelA (p65), RelB, c-Rel, NF-κB1, and NF-κB2, and their transcriptional activities are tightly controlled to ensure their transient signaling in response to specific stimuli. The NF-κB signaling cascade is usually triggered by sensor molecules, such as toll-like receptor (TLR) family proteins. These proteins can identify the presence of a wide range of microorganisms and then transmit that information through phosphorylation relays to downstream kinases, which eventually culminate at the I-κB kinase (IKK). IKK activates NF-κB via phosphorylation of inhibitory I-κB proteins (primarily I-κBα), which leads to its ubiquitylation and degradation by the 26S proteasome complex and allows NF-κB to enter the nucleus. I-κB is induced by NF-κB to function in a negative feedback loop that terminates NF-κB signaling. Aberrant activation of NF-κB has been linked to several pathological features such as allergic responses, autoimmune diseases, septic shock, and carcinogenesis in a variety of organs [4].

In addition to I-κB, deubiquitinase A20 (also referred to as TNFα-induced protein 3 or TNFAIP3) targets important signaling intermediates upstream of I-κB to terminate NF-κB activation [5,6]. A20 cleaves Lys63 (K63)-linked polyubiquitin chains on

overlapping substrates, such as E3 ubiquitin ligase TRAF6 and adaptor molecule RIP1, with the help of the substrate-specific adaptor Tax1-binding protein 1 (Tax1bp1 [7,8]). Tax1bp1 intrinsically regulates NF-κB by recruiting A20 to the target molecules to remove their polyubiquitin chains, which play important roles in their assembly into the IKK complex [8,9]. Deficiencies in A20 or Tax1bp1 lead to uncontrolled and spontaneous systemic inflammation in mice as a result of unchecked NF-κB signaling [8,10].

Tax1bp1 was originally identified as a host cell factor that binds to the encoded protein of human T-lymphotropic virus type 1 (HTLV-1), known as Tax1 [7]. Tax1 is a potent activator of NF-κB and a major pathogenic factor in HTLV-1 associated diseases (HAD), such as HTLV-1 associated myelopathy (HAM) or HTLV-1 uveitis (HU [11]), and adult T-cell leukemia (ATL [12]). Tax1 interrupts the ability of Tax1bp1 to connect to and recruit A20 to target molecules and thus evokes persistent NF-κB activation [13,14]. Tax1 also activates NF-κB by binding to the NF-κB essential modulator (NEMO), a regulatory subunit of IKK [15]. The aberrant activation of NF-κB in HADs can therefore be attributed to Tax1, which leads to Tax1bp1 dysfunction, over-activation of IKK, or both. Epidemiological studies provide support for a close link between HTLV-1 infection and HAD or other inflammatory diseases such as Sjögren's syndrome [16], vascular dementia [17], and atherosclerosis [18]. Moreover, recent accumulating evidence strongly suggests that several mutations in the *A20* locus are primarily responsible for the development of Crohn's disease, rheumatoid arthritis, systemic lupus erythematosus, psoriasis and type 1 diabetes [19].

For research purposes, we established *TAX1BP1*-deficient (-KO) mice, which display exacerbation of inflammation (characterized as valvulitis and dermatitis) in an age-dependent manner in addition to functional inadequacies manifested in growth retardation and premature death [8]. To elucidate the molecular mechanisms underlying the manifestation of inflammatory symptoms and their link to premature or possible cardiac abnormalities induced by *TAX1BP1*-deficiency, we performed a series of pathological evaluations using *TAX1BP1*-KO mice: (1) laser capture microdissection (LCM)- and gene expression microarray-based profiling of the mitral valves, which was reevaluated using real-time polymerase chain reaction (RT-PCR); (2) multiplex cytokine and chemokine quantitation in sera on systemic inflammatory constitution; (3) histochemical and electron microscopic analyses of multiple pathogenic foci; and (4) antibiotic treatments and cross experimentation with *MyD88*-deficient mice [20] to examine the role of commensal microbiota in the pathogenesis of *TAX1BP1*-KO mice.

From our experimental data, we conclude that systemic inflammation and cardiac structural abnormalities in *TAX1BP1*-KO mice originated from commensal microbiota, which are usually harmless in nature. Furthermore, these results indicate a potential risk to asymptomatic HTLV-1 carriers, which should be addressed by further clinical research.

Table 1. Primer sequences.

SAA3	**acagcctctctggcatcg**	**atgctcggggaactatgat**	**#26**
TAX1BP1	ataaaaatgtgtaatagtcacgagcag	cactccaaagattgggttgg	#56
EFCAB2	tgtccgtcgtggctatgac	cctgcttcaccaccttcttg	#80
GAPDH	tcgaccatgaatcgaataataca	tgcagctctccttcagtcg	#89

doi:10.1371/journal.pone.0073205.t001

Table 2.

IL6	**gctaccaaactgga tataatcagga**	**ccaggtagctatgg tactccagaa**	**#6**
CXCL1	agactccagccacacactccaa	tgacagcgcagctcattg	#83
GAPDH	tcgaccatgaatcgaataataca	tgcagctctccttcagtcg	#89

doi:10.1371/journal.pone.0073205.t002

Materials and Methods

Animals

TAX1BP1-KO mice having replaced their exon 17 region with CMV-driven NEO gene in reverse orientation [8] and their wild-type (WT) littermates as controls were analyzed throughout the experiment. These strains are maintained as F9 or advanced generations of C57BL/6CrSlc or the original 129/+ Ter/SvJcl. *MyD88* deficient mice are kind gifts from professor Hitoshi Nakashima from Fukuoka University [21]. Homozygous *TAX1BP1*-KO mice were crossbred with homozygous *MyD88*-KO background to generate *MyD88/TAX1BP1*-KO mutants. Each of the targeted loci was evaluated by PCR. These mice were bred and maintained under specific pathogen-free (SPF) conditions at the animal facility of Oita University Faculty of Medicine. All the mice related manipulations were performed with protocols approved by the animal ethics committee at the Oita University (Justified numbers, daily care, treatment and euthanasia procedures).

Laser capture microdissection

Three mitral valves from 8 or 16 week old (-wk) male *TAX1BP1*-KO and their WT littermates were collected by Arcturus XT laser capture microdissection system according to a manufacture's directions.

RNA Isolation and gene expression microarray analysis

Total RNAs were purified from the mitral valves using RNeasy mini kit (Qiagen). RNA quantity and purity were evaluated using a NanoDrop 2000 (NanoDrop Technologies). All RNA samples were labeled, linearly amplified by Low Input Quick Amp Labeling Kit and RNA Spike-In Kit then analyzed with Whole Mouse Genome Microarray Kit (Agilent). Signal intensities were quantitated with laser confocal scanner and analyzed with Feature Extraction software (Version 10.7.3.1, Agilent) and R statistical package (Version 2.15.1). Probe set data were median-normalized per chip. Empirical Bayesian method controlling for false discovery rate (FDR: <3% and logFC >1.0 [22]) for comparison of differentially expressed between *TAX1BP1*-KO mice and their WT. Principal Component Analysis (PCA) for the systematic trend examination, heatmaps by R Software and volcano plot analysis were applied to identify the single mRNA differentially expressed in *TAX1BP1*-KO mice (log2-fold expression change on the x-axis and t test p values on the y-axis, negative log). Each dot represents a single probe. The complete gene expression dataset can be viewed in the Gene Expression Omnibus (GEO) repository accession number GSE43932 (www.ncbi.nlm.nih.gov/geo/query/acc.cgi?acc = GSE43932).

Quantitative real time-polymerase chain reaction (RT-PCR)

Taqman quantitative RT-PCR was performed to validate a subset of genes. Random hexamer-primed cDNA templates were

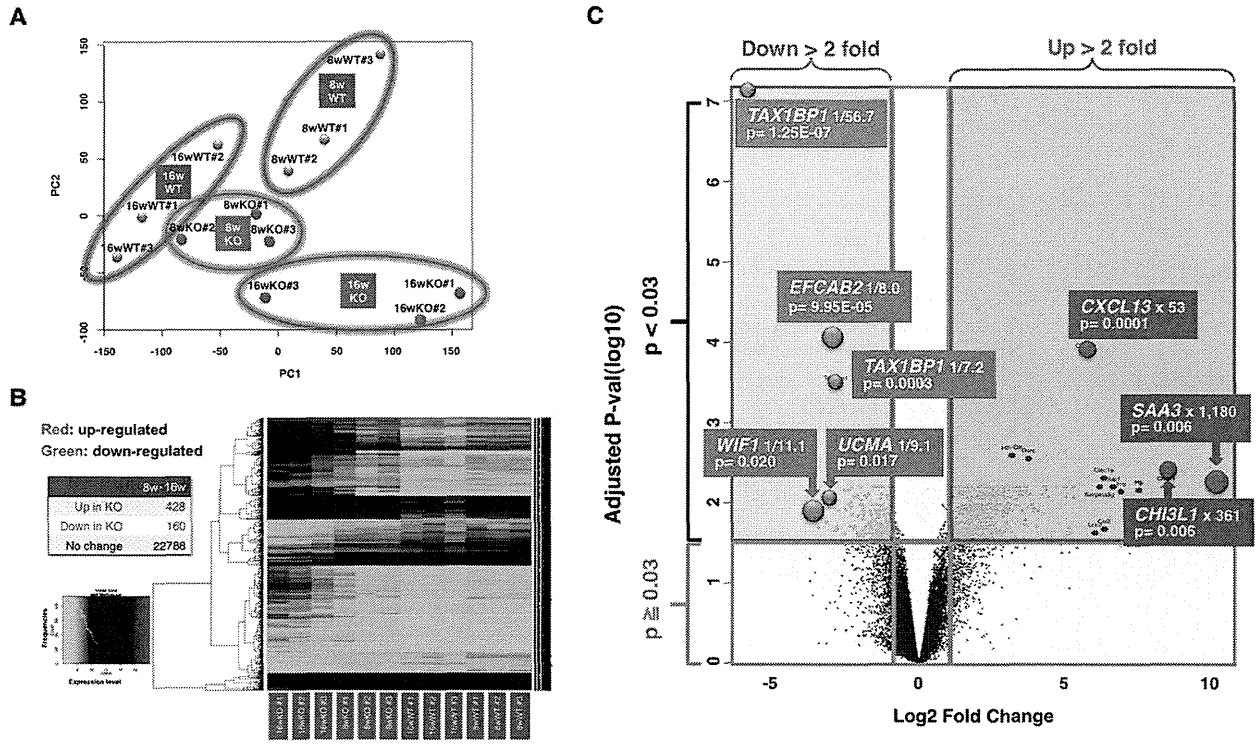

Figure 1. Elevated inflammatory profiles in the multiple organs of *TAX1BP1*-KO mice. Mitral valve tissues from either 8 or 16 week old (-wk) *TAX1BP1*-KO mice or their wild-type littermates were collected by Arcturus XT LCM system and total RNAs were prepared by RNeasy mini kit (Qiagen). Each cDNA pool was generated from the individual RNA sample and gene expression profiles were evaluated using Whole Mouse Genome Microarray Kit (Agilent). **A**) Principal component analysis (PCA) by conditions was performed on R statistical package (Version 2.15.1) and represented as a scatterplots of whole gene expression profiles of 8- or 16-wk *TAX1BP1*-KO mice (8wKO #1- #3 or 16wKO #1-#3, surrounded by red circles) and their WT littermates (8wWT #1- #3 or 16wWT #1-#3, blue circles). The PCA plot showed that samples clustered based on their genetic backgrounds. Data represent n = 12. Component % variance; PC1 = 34.95%, PC2 = 19.48%. **B**) Heat map representation of differentially expressed genes in the mitral valves from either 8- or 16-wk *TAX1BP1*-KO mice or their WT littermates. 588 genes were differentially expressed in *TAX1BP1*-KO vs. WT littermates ($P<0.03$). Each column represents the expression profile of either the *TAX1BP1*-KO mice or WT littermates. Red and green colors indicate high and low expression levels, respectively, relative to the mean (see color bar). **C**) Volcano plot analysis of microarray revealed that 588 probes were significantly expressed more than 2-fold vs control. Red and green areas indicate significant increasing and decreasing changes in gene expression ($p<0.03$).
doi:10.1371/journal.pone.0073205.g001

synthesized from purified (RNAs ReverTra Ace®, TOYOBO). The output of RT-PCR reactions were quantitated with Light-Cycler® R 480 System (Roche). Primer sequences were listed in Table 1. Each reaction was run in triplicate with endogenous control *GAPDH* on the same reaction plate.

Multiple cytokine & chemokine quantitation

The 3-, 8-, 16- and 32-wk male *TAX1BP1*-KO and their WT littermates were anesthetized and an aliquot of serum (12.5 μl) from heart blood were collected (n = 5/groups). Quantitation of 23 cytokines and chemokines was performed by a multiplex ELISA system (Bio-Plex, BioRad) and analyzed by the Bio-Plex Manager Software 6.1 (Bio-Rad) with a five-parameter curve-fitting algorithm for standard curve calculations.

Immunohistochemistry

A standard avidin-biotin-peroxidase technique or hematoxylin and eosin (HE) staining were employed for Saa3 and I-κBα staining or morphological observation of heart, liver and skin tissues of 8- or 16-wk male *TAX1BP1*-KO and their WT littermates (n = 5/groups). Rabbit polyclonal anti-Saa3 antibody (ab59736, abcum), rabbit monoclonal anti-I-κBα antibody (ab32518, abcum) or control antibody for visualization of antigens with EnVision + System-HRP Labelled Polymer Anti-Rabbit (Dako). DAB + Liquid (Dako) for positive staining and Mayer's hematoxylin solution for counterstaing. Images were captured with BZ-9000 (KEYENCE). Mice whole eye sections were examined with anti-T6BP antibody (ab22049, abcam). Anti-IgG (H+L), rabbit, goat-poly, DyLight 649 (KPL) was used as secondary antibodies.

Electron microscopy

For transmission electron microscopy (TEM), mitral valve, atrioventricular node, sinoatrial node and papillary muscles of the left ventricle of 8-, 16-, 60-wk male *TAX1BP1*-KO and their WT littermates (n = 3/groups) were fixed with 2.5% glutaraldehyde/2% paraformaldehyde in a 0.1 M cacodylate buffer (pH7.4) for 3 hr or longer at 4°C. After a washing in the cacodylate buffer, specimens were postfixed in 2% osmium tetroxide in cacodylate buffer for 2 hr, washed with cacodylate buffer, dehydrated with ethanol and embedded in epoxy resin. Thin section specimens (80–90 nm) were then stained with uranyl acetate and lead cystate and examined with TEM H-7650 (at 80 kV, HITACHI).

Western blotting

Tissues from liver, heart, spleen, muscle, lung, skin, stomach and brain from WT BL6 were lysed with Co-IP buffer [23] and equal amounts of protein solutions (20 μg/lane) were separated by

Table 3. Gene symbol, gene description, fold change and p-value for all genes up-regulated by >20-fold in *TAX1BP1*-KO mice.

SYMBOL	DESCRIPTION	Fold activation	adj.P. Val
SAA3	Serum amyloid A 3	1179.5	0.006
CHI3L1	Chitinase 3-like 1	361.0	0.006
HP	Haptoglobin	187.2	0.007
IL1B	Interleukin 1 beta	121.9	0.007
SPP1/OPN	Secreted phosphoprotein 1/Osteopontin	100.7	0.006
CCL2/MCP1	Chemokine (C-C motif) ligand 2/Monocyte chemotactic protein-1	81.7	0.021
CLEC7A/DECTIN1	C-type lectin domain family 7, member a/Dectin-1	81.0	0.005
SERPINA3G	Serine (or cysteine) peptidase inhibitor, clade A, member 3G	73.0	0.006
LCN2	Lipocalin 2	65.3	0.024
SAA1	Serum amyloid A 1	61.1	0.024
CXCL13/BLC	Chemokine (C-X-C motif) ligand 13/B lymphocyte chemo-attractant	52.9	0.0001
SLPI	Secretory leukocyte peptidase inhibitor	39.8	0.009
CLEC4D/DECTIN2	C-type lectin domain family 4, member d	39.6	0.006
TIMP1	Tissue inhibitor of metalloproteinase 1	37.4	0.024
CCL17/TARC	Chemokine (C-C motif) ligand 17/Thymus and activation regulated chemokine	35.2	0.020
CCL7	Chemokine (C-C motif) ligand 7	33.8	0.025
LGALS3/GALECTIN3	Lectin, galactose binding, soluble 3/Galectin-3	33.5	0.008
SIRPB1A	Signal-regulatory protein beta 1A	33.3	0.006
CHL1	Cell adhesion molecule with homology to L1CAM	32.4	0.027
CCL8	Chemokine (C-C motif) ligand 8	31.4	0.006
BCL2A1B	B-cell leukemia/lymphoma 2 related protein A1b	27.0	0.006
MEFV	Mediterranean fever	26.7	0.006
PLAC8	Placenta-specific 8	21.7	0.008
ZMYND15	Zinc finger, MYND-type containing 15	20.6	0.007
ITGAX	Integrin alpha X	20.0	0.006

Statistical significance ($p<0.03$) was calculated using the Empirical Bayesian method controlling for false discovery rate (FDR) <3% and logFC >1.0 on R statistical package (Version 2.15.1). Fold change represents a comparison between mean normalized signal intensity for control ($n=6$) versus *TAX1BP1*-KO mice ($n=6$).
doi:10.1371/journal.pone.0073205.t003

SDS-PAGE and transferred to immobilion membranes (Millipore) and incubated with primary antibodies, T6BP Antibody (sc-15274, Santa Cruz) or anti-Tubulin antibody (ab6160, abcum) and secondary antibodies, donkey anti-goat IgG-HRP (sc-2033, Santa Cruz) or ZyMAX^{TM} Goat anti-Rat IgG(H+L) HRP conjugate (81–9520, invitrogen) and visualized with ECL Western Blotting Detection System (GE Healthcare Lifesciences) and high-performance chemiluminescence film.

Evaluation of physiological responses to LPS-stimulation

200 μg of *Salmonella typhimurium* lipopolysaccharide (LPS, Sigma) in 100 μl sterile pyrogen-free saline were injected into the footpads of *TAX1BP1*-KO or WT littermates (n = 4/groups). Tissue lysates were prepared from eyeball and the expression of Tax1bp1, I-κBα (anti-I-κBα rabbit mAb, #4812, Cell Signaling Technology) and Tubulin were evaluated by western blotting. Total RNAs were prepared from eyeballs of *TAX1BP1*-KO or WT littermates (n = 4/groups). Taqman quantitative RT-PCR was performed as described above (See Table 2).

Sera from peripheral blood samples were collected 0, 6 and 12 hr after LPS injection and quantitated with Bio-Plex Pro^{TM} Mouse Cytokine 23-plex kit.

Enzyme-linked immunosorbant assay (ELISA)

The amounts of Saa3 and Cxcl13 Sera from 16-wk mice (n = 5/group) were measured with MOUSE SAA-3 ELISA KIT (Millipore) and Mouse CXCL13/BLC/BCA-1 Quantikine ELISA Kit (R&D Systems).

Table 4. Gene symbol, gene description, fold change and p-value for all genes down-regulated by >5 fold in *TAX1BP1*-KO mice.

SYMBOL	DESCRIPTION	Fold suppression	adj.P. Val
TAX1BP1	Tax1 (human T-cell leukemia virus type I) binding protein 1	56.7	0.0000001
WIF1	Wnt inhibitory factor 1	11.1	0.0205
UCMA	Upper zone of growth plate and cartilage matrix associated	9.1	0.0173
EFCAB2	EF-hand calcium binding domain 2	8.0	0.0001
FAM107A/DRR1	Family with sequence similarity 107, member A/down-regulated in renal cell carcinoma 1	7.6	0.0219
TSC22D3	TSC22 domain family, member 3	7.3	0.0197
TAX1BP1	Tax1 (human T-cell leukemia virus type I) binding protein 1	7.2	0.0004
MAP3K6/ASK2	Mitogen-activated protein kinase kinase kinase 6	7.1	0.0212
6030422H21RIK	RIKEN cDNA 6030422H21 gene	6.8	0.0124
TSC22D3	TSC22 domain family, member 3	5.9	0.0240
PENK	Preproenkephalin	5.7	0.0119
CNTFR	Ciliary neurotrophic factor receptor	5.3	0.0104
COL11A2	Collagen, type XI, alpha 2	5.3	0.0069
RXFP3	Relaxin family peptide receptor 3	5.2	0.0197
NRXN1	Neurexin I	5.1	0.0110
CYTL1	Cytokine-like 1	5.0	0.0099

Statistical significance ($p<0.03$) was calculated using the Empirical Bayesian method controlling for false discovery rate (FDR) <3% and logFC >1.0 on R statistical package (Version 2.15.1). Fold change represents a comparison between mean normalized signal intensity for control (n = 6) versus *TAX1BP1*-KO mice (n = 6).
doi:10.1371/journal.pone.0073205.t004

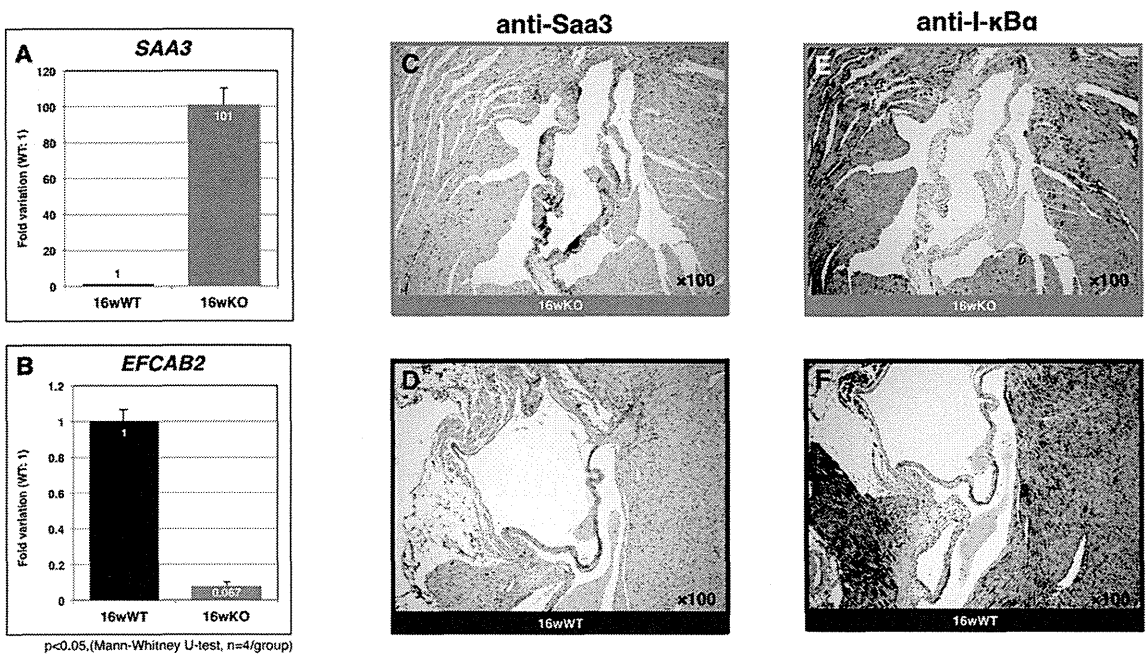

Figure 2. Validation of genes and proteins identified their expression alteration in the mitral valves of *TAX1BP1*-KO mice. RT-PCR validation of genes identified their expression alteration in the mitral valves of *TAX1BP1*-KO mice, **A**) *SAA3* **B**) *EFCAB2* respectively. Gray bar: *TAX1BP1*-KO, black bar: WT. Mitral valve specimens were prepared from 16-wk *TAX1BP1*-KO mice or their WT littermates and stained by anti-Saa3 antibody (**C** and **D**) or anti-I-κBα antibody respectively (**E** and **F**).
doi:10.1371/journal.pone.0073205.g002

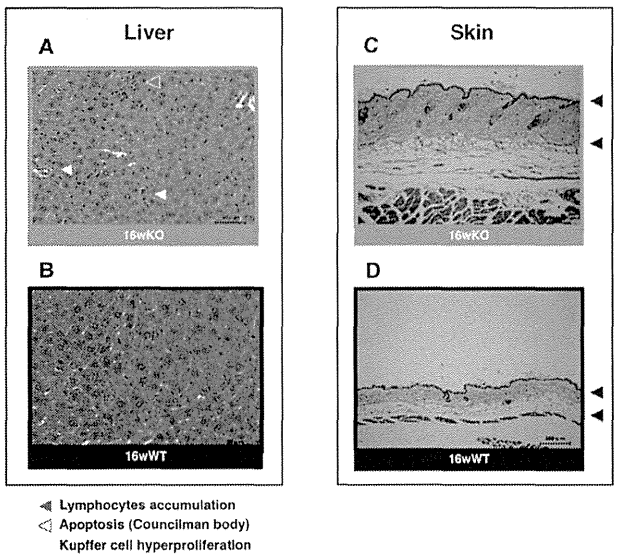

Figure 3. Inflammatory properties in the multiple organs of *TAX1BP1*-KO mice. The morphologic and functional alterations of the environments of liver (**A** and **B**) and skin (**C** and **D**) were also examined with HE-staining. Red and white triangles indicate accumulated lymphocytes and Councilman bodies respectively.
doi:10.1371/journal.pone.0073205.g003

Telemetric electrocardiogram (ECG)

Sixteen week old male *TAX1BP1*-KO or WT littermates with or without antibiotic treatment (n = 5/group) were monitored with telemetric electrocardiogram. Telemetric transmitter was implanted into the back of mice under aseptic conditions and the muscle layers and the skin were closed with resorbable sutures. Data were acquired at least 72 hour after the implantation with a receiver placed under the cage and a full-disclosure 72 hour recordings were analyzed off-line and the P-Q intervals were evaluated.

Antibiotic treatment

TAX1BP1-KO or WT littermate male mice were first raised with the normal diets and water for 4 weeks, and then, antibiotic group (n = 5/groups) received ampicillin (1 g/L; Wako), vancomycin hydrochloride (500 mg/L; Wako), neomycin trisulfate salt hydrate (1 g/L; Sigma-Aldrich), and metronidazole (1 g/L; Wako) in drinking water for 12 weeks [24]. The non-antibiotic controls were equally raised and maintained except for antibiotics treatment. Both groups of mice were maintained in flexible film isolators under a strict 12-hour light cycle and fed an autoclaved chow diet and tap water ad libitum. Germ free status was verified regularly by ensuring negative cultures from mouse feces in three media types: nutrient agar (Nissui), pourmedia sheep blood agar M70 (Eiken), and Sabouraud agar (Nissui). Microbial colonies were counted after incubation at 37°C for 48 hour (aerobes) or 72 hour (anaerobes). Both groups of mice were anesthetized and sacrificed at the end of 16 weeks experimental period. Daily fluid consumption, body weight, liver function (ALT, AST), renal

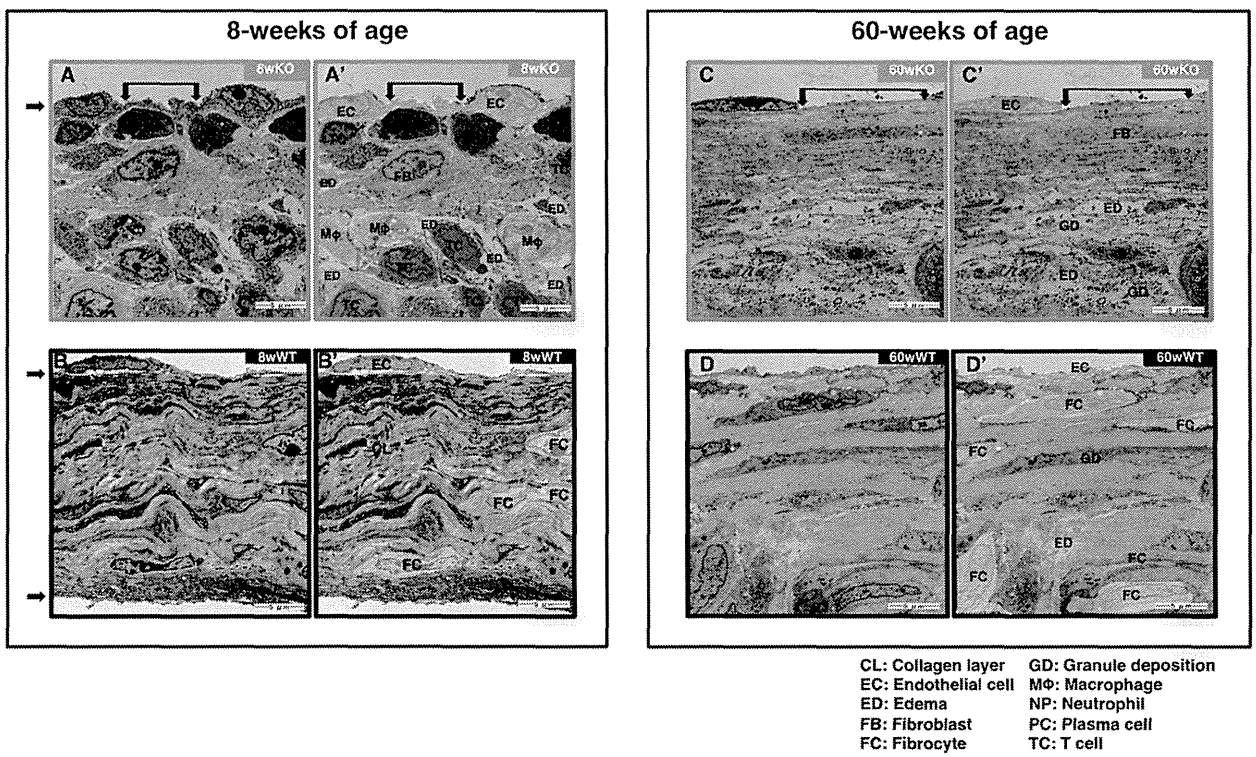

Figure 4. Massive infiltration of inflammatory cells causes severe tissue lesion in the mitral valves of *TAX1BP1*-KO mice. Electron microscopy examinations on the mitral valves of 8-, 16- and 60-wk *TAX1BP1*-KO mice (**A:** 8wKO, and **C:** 60wKO) and their WT littermates (**B:** 8wWT and **D:** 60wWT). See Figure S1 for details. Each panel was duplicated with colorized areas in specific cell types and abbreviated descriptions (Fig. 4A' to 4D'). Abbreviations, CL: Collagen layer; EC: Endothelial cell; ED: Edema; FB: Fibroblast; FC: Fibrocyte; GD: Granule deposition; MΦ: Macrophage; NP: Neutrophil; PC: Plasma cell; TC: T cell.
doi:10.1371/journal.pone.0073205.g004

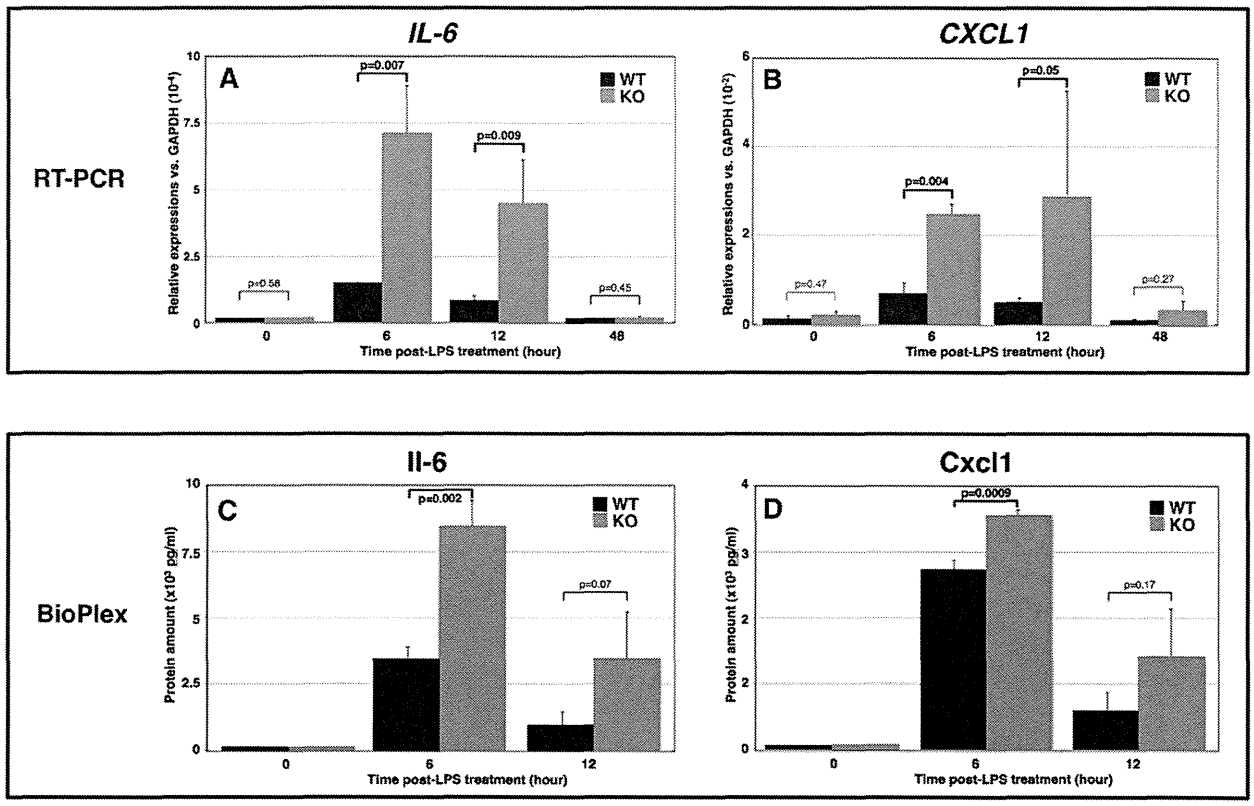

Figure 5. Enhanced expression of inflammatory genes after the LPS-stimulation to *TAX1BP1*-KO mice. 200 μg of *Salmonella typhimurium* lipopolysaccharide (LPS) in 100 μl sterile pyrogen-free saline were injected into a right footpads of *TAX1BP1*-KO or WT littermate mice. At the time 2, 6, 12, 24 and 48 hour post-injection (PT), each group of mouse were euthanized and tissues including serum, lymphocytes and eyes were collected. **A**) LPS-triggered induction of Tax1bp1 in eye tissue was monitored. Ten μg of cell lysates from WT BL6 mice at 2, 6, 12, 24 and 48 hour PT of LPS were probed with anti-Tax1bp1, -I-κBα and -Tubulin antibodies. **B, C**) Total RNAs of eye tissues from at 6, 12 and 48 hour PT of LPS to *TAX1BP1*-KO or WT littermates and their untreated controls were prepared and the expressions of *IL-6* and *CXCL1* were quantitated with RT-PCR. **D, E**) Sera from at 6, 12 and 48 hour PT of LPS to *TAX1BP1*-KO or WT littermates and their untreated controls were collected and the amount of Il-6 and Cxcl1 were quantitated with multiplex ELISA system (BioRad). Gray bar: *TAX1BP1*-KO, black bar: WT littermate.
doi:10.1371/journal.pone.0073205.g005

function (BUN), nutritional status (TG, GLU, TP) and spleen weight (After 10% formalin fixation) were examined. Caecum surface area was measured with Image J (NIH). In general, there were no particular adverse effects on mice through antibiotic treatment.

Statistical analysis

All numerical data are expressed as means ± SD. Statistical significance was assessed by Student's two-tailed t-test. In the case of ELISA, Statistical analyses were performed by one-way analysis of variance and Steel-Dwass test. Data were considered significant when $P<0.05$.

Results

LCM- and gene expression microarray array-based profiling of the mitral valves in *TAX1BP1*-KO mice and reevaluation by RT-PCR and immunostaining

We have previously observed that the mRNA expression level for several inflammatory cytokines, including IL-1β and TNFα, increases in the cardiac and skin tissues of *TAX1BP1*-KO mice; more importantly, these mice showed mitral valvulitis and premature death compared to their wild-type (WT) littermates. However, the underlying mechanisms involved in these processes remain unknown [8].

To date, information on variations in the levels of gene expression in regions of the heart (more specifically, the mitral valves) showing inflammation in *TAX1BP1*-KO mice is still lacking. This pathologic event is thought to be linked to premature death, which might be brought on by cardiac failure. In the current study, we employed LCM- and gene expression microarray-based techniques to obtain detailed information on the levels of gene expression in organs showing pathological changes. Total RNA was extracted from three independent tissue samples obtained from the mitral valves of 8- or 16- week-old (-wk) male (WT and TAX1BP1-KO) mice by using LCM, which was followed by total RNA extraction. Then, global mRNA expression profiles were analyzed by an Agilent gene expression microarray.

Principle component analysis, using two principle components, was conducted and the results were represented by a scatterplot (Fig. 1A). The data showed that the results for all samples from *TAX1BP1*-KO mice clearly deviated from those for control mice, indicating detectable differences in the gene transcription patterns of the two genetic backgrounds. A gene list was compiled on the basis of normalization and statistical analysis ($P<0.03$, logFC >1.0). Using these criteria, alterations in 588 gene expression profiles were identified. Unsupervised hierarchical clustering

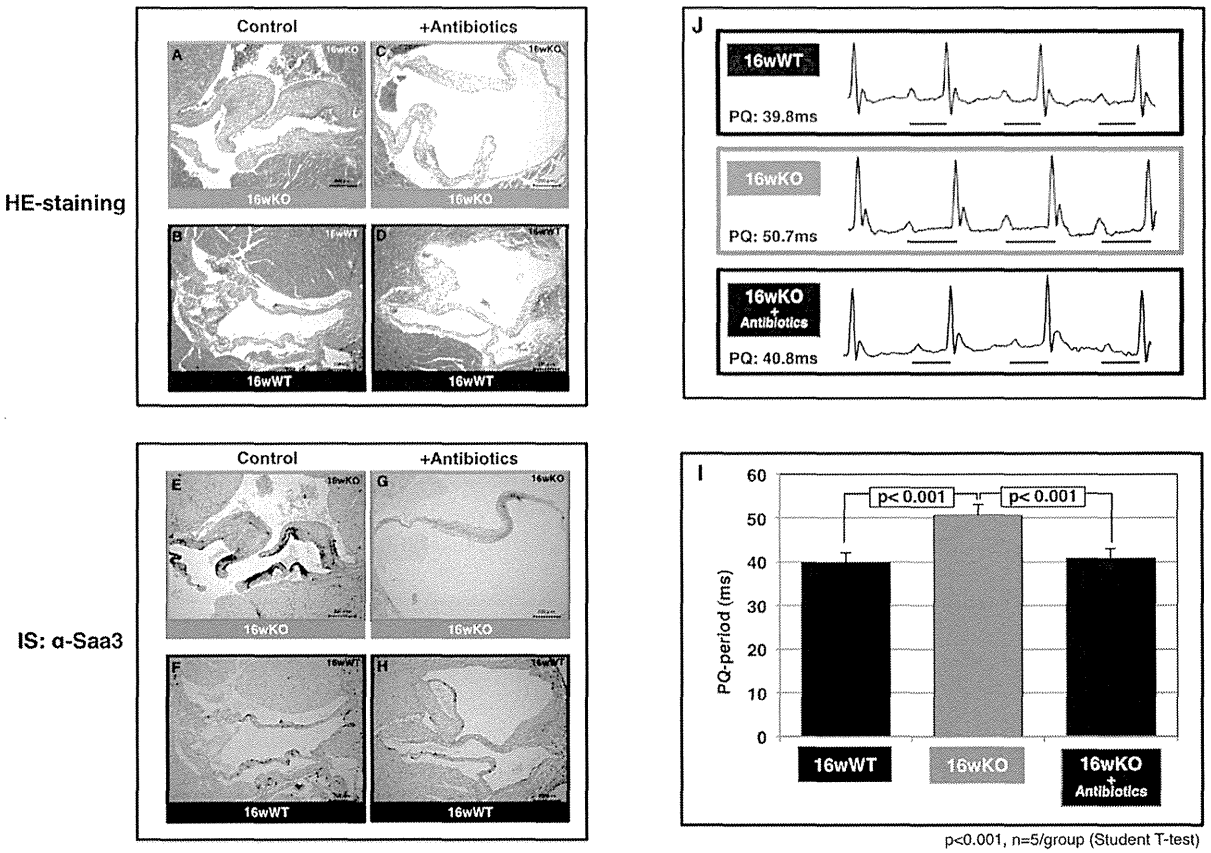

Figure 6. Amelioration of inflammatory valvulitis and conduction disturbance after the antibiotics treatment on *TAX1BP1*-KO mice. *TAX1BP1*-KO or WT littermate mice (male) were first raised with the normal diets and water for 4 weeks, and then, antibiotic treatment group (**C**, **D**, **G** and **H**, n = 5/group) provided ampicillin (1 g/L; Wako), vancomycin Hydrochloride (500 mg/L; Wako), neomycin trisulfate salt hydrate (1 g/L; Sigma-Aldrich), and metronidazole (1 g/L; Wako) in drinking water for 12 weeks based on a protocal of the commensal depletion (Rakoff-Nahoum S., Cell 2004). The non-antibiotics controls (**A**, **B**, **E** and **F**, n = 5/group) were equally raised and maintained except for antibiotics treatment. Each group of mice were anesthetized and sacrificed at the end of 16 weeks experimental period and histochemical representatives of each group were displayed with HE-staining (**A** to **D**) or anti-Saa3 immuno-staining (IS, **E** to **H**). **I**). Heart rhythms of 16-week-old *TAX1BP1*-KO treated with antibiotics over 12 weeks (male, n = 5/group) were monitored with telemetric electrocardiogram (12-lead ECG). **J**) The average values of PQ-intervals were compared with those of untreated *TAX1BP1*-KO mice and their WT littermates.
doi:10.1371/journal.pone.0073205.g006

analysis (Cluster 3.0; Stanford University) of the 588 genes resulted in the separation of all *TAX1BP1*-KO from their paired WT controls. In total, 428 probes were upregulated and 160 were downregulated for a total of 24,000 genes (Fig. 1B). We then applied volcano plot analysis to identify the differences in mitral valve mRNA expression in *TAX1BP1*-KO mice and the controls.

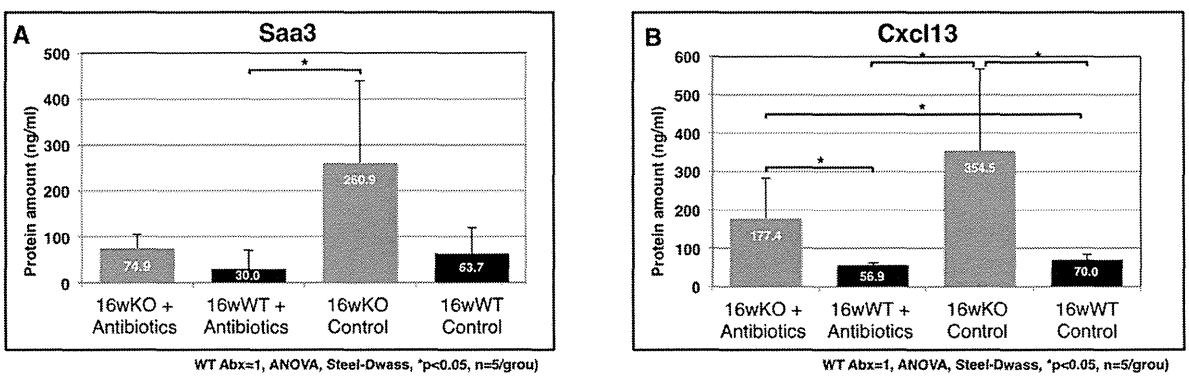

Figure 7. Reduction of the Saa3 and Cxcl1 expression in the sera of TAX1BP1-KO mice after the antibiotics treatment. ELISA quantitation of Saa3 (**A**) or Cxcl13 (**B**) of the sera on four groups were performed. Gray bar: *TAX1BP1*-KO mice, black bar: WT littermates (n = 5/group).
doi:10.1371/journal.pone.0073205.g007

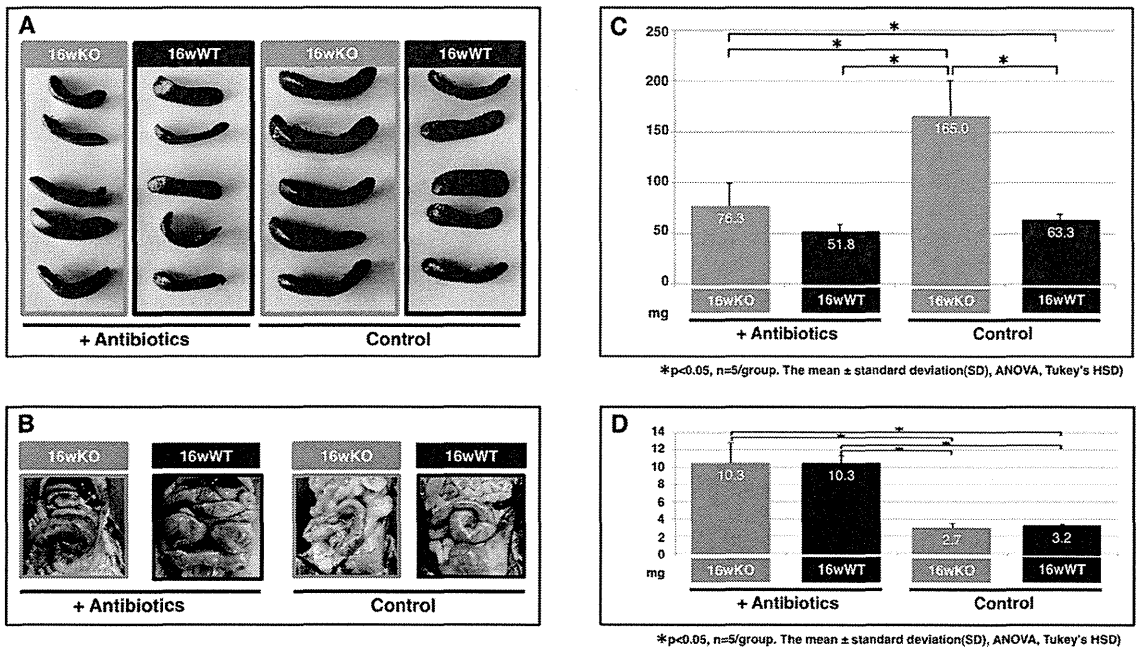

Figure 8. Splenic hypertrophy of *TAX1BP1*-KO mice and its cancellation by antibiotics treatment. Examinations on the spleen volume (**A**) and the area of cecum (**B**) were performed. The average values of spleen volumes (**C**) and cecum areas (**D**) were displayed (n = 5/group).
doi:10.1371/journal.pone.0073205.g008

The plot showed a log2-fold change in mRNA expression between the two groups on the x-axis and the negative log of the t-test p-values on the y-axis. Each gene was represented by a single dot. Using the plot, we identified 588 probes that showed a more than 2-fold differential expression of mRNA when compared to the controls ($p<0.03$, Fig. 1C).

Tables 3 and 4 list the gene symbols, gene descriptions, fold changes, and p-value for all genes upregulated by more than 20-

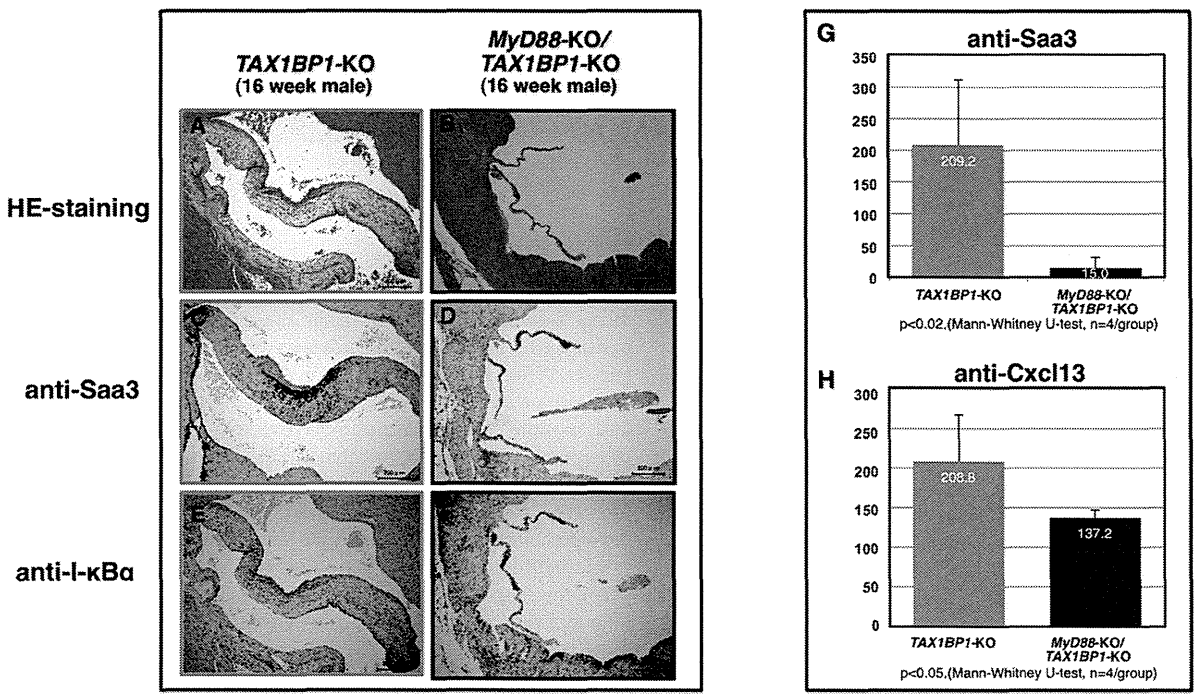

Figure 9. Cancelation of valvulitis in the *MyD88/TAX1BP1* double-KO mice. The HE-staining (A, B) and immunostaining of Saa3 (C, D) and I-κBα (E, F) were compared between *TAX1BP1*-KO and *MyD88/TAX1BP1*-KO mice. ELISA quantification of Saa3 (I) and Cxcl13 on the sera of both genetic background.
doi:10.1371/journal.pone.0073205.g009

fold or downregulated by more than 5-fold. Most of the upregulated genes were primarily involved in inflammation. The gene showing the highest level of induction, *SAA3*, (i.e., 1,180 fold induction) along with *SAA1* (i.e., 61 fold, 10th induction) are well-known inflammatory markers in patients with autoimmune disease, chronic infection and cancer [25]. *SAA3* is also hyper-induced at the site of injury [26], inflammation [27] in mice experimental models. Additionally, genes related to immune modulation, including pathogen recognition, inflammation, chemotaxis [28–30], or tissue adhesion, degeneration and rearrangement [31,32] were induced in the mitral valves of *TAX1BP1*-KO mice. The characteristics of the downregulated genes also suggested the link between inflammation and tissue degeneration (Table S1); for example, such as *WIF1*, a Wnt signaling suppressor; *UCMA*, a gene associated with cartilage development [33–35]. *EFCAB2* is a functional partner of the voltage-gated Ca^{2+} channel [36]. *TSC22D3* (also known as *GILZ*: a *G*lucocorticoid *I*nduced *L*eucine *Z*ipper) is an IL-10-inducible immune suppressor [37].

We further confirmed the microarray results for *SAA3* and *EFCAB2* by using RT-PCR (Fig. 2AB and Figure S1) and for Saa3 (induction) or I-κBα (reduction) by using immunostaining for mitral valve samples from 16-wk *TAX1BP1*-KO mice (Fig. 2C to F). In addition to these microenvironmental changes, broad-spectrum inflammatory effects, such as lymphocyte accumulation, apoptotic Councilman body formation, and Kupffer cell hyper proliferation in the hepatocyte (Fig. 3A), and thickening of the inflamed skin (Fig. 3C), were observed in 16-wk *TAX1BP1*-KO mice. Multiplex ELISA quantitation of the sera for homozygous or heterozygous *TAX1BP1*-KO and their WT littermates showed age-dependent development of systemic inflammation (Table S1). The levels of Il-6 and Cxcl1 were elevated more than 10- fold in the homozygous *TAX1BP1*-KO mice.

Massive infiltration of inflammatory lymphocytes in the mitral valves of *TAX1BP1*-KO mice

To obtain more detailed images of critical sites of inflammation, tissues obtained from the mitral valves of *TAX1BP1*-KO mice and their WT littermates at varying time points were examined with electron microscopy (Fig. 4). Surprisingly, the mitral valves *TAX1BP1*-KO mice showed extensive infiltration of lymphocytes, macrophages and neutrophils and tissue degeneration at only 8 weeks of age (Fig. 4A and 4A'), whereas the mitral valves of the WT littermates exhibited healthy collagen layers (Fig. 4B and 4B'). Extensive disruption of collagen layers and edema were observed at 60 weeks of age for *TAX1BP1*-KO mice (Fig. 4C, 4D and 4C', 4D').

Enhanced inflammatory responses in *TAX1BP1*-KO mice after the LPS-stimulation

In addition to the chronic inflammation, the acute-phase inflammatory response of *TAX1BP1*-KO mice was also examined. *Salmonella typhimurium* lipopolysaccharide (LPS) was injected into the footpads of *TAX1BP1*-KO mice and their WT littermates. Then, the mice were monitored, and the effects were recorded. We examined the kinetics of mRNA expression in those same eye tissues (Fig. 5A, B: tissue specific) and the translational products in the sera (Fig. 5C, D: systemic) of *IL-6* and *CXCL1* were monitored. Both data clearly indicate that a deficiency in *TAX1BP1* causes significantly enhanced inflammation in responses to LPS in *TAX1BP1*-KO mice.

Amelioration of the inflammatory symptoms and the cardiac conduction defect of *TAX1BP1*-KO mice by antibiotic treatment and simultaneous *MyD88* deficiency

Microbial infections spontaneously cause severe endothelial inflammatory diseases such as rheumatic fever and Kawasaki disease [38]. At the subcellular level, modulation of the threshold of immune cell activation, differentiation, and immune cell activity in response to non-self or self antigens in *TAX1BP1*-KO mice (Fig. 1 and Tables 3 and 4) might evoke autoimmune profiles and heart dysfunction. To test this hypothesis, we examined the link between the commensal microbiota and mitral valvulitis and endocarditis in *TAX1BP1*-KO mice. When the mice were 4 weeks old, antibiotics were orally administered to all subjects over a 12-week period. The telemetric electrocardiogram profiles then sacrificed for the pathologic examination. Inflammatory hypertrophy (Fig. 6A) and extensive Saa3 staining (Fig. 6E) of the mitral valves in *TAX1BP1*-KO mice were abolished with antibiotic treatments (Fig. 6C and G); no changes were observed in their WT littermates (Fig. 6B, D, F and H). Extended PQ-intervals observed by telemetric electrocardiogram in *TAX1BP1*-KO mice (Fig. 6I, middle panel) were alleviated with the administration of antibiotics (Fig. 6I, bottom panel). The statistical significance of the differences in the PQ-intervals was tested (Fig. 6J). The antibiotic regimen also reduced the secretion of Saa3 and Cxcl13 in the sera of *TAX1BP1*-KO mice (Fig. 7A, B), and splenic hypertrophy of *TAX1BP1*-KO mice was almost nonexistent (Fig. 8A). Typical cecum thickening due to antibiotic treatment was also confirmed (Fig. 8B), and fecal microbes were completely disappeared under these conditions (data not shown). If the eradication of microbiota is the main reason for the amelioration of the symptoms in *TAX1BP1*-KO mice, we hypothesized that the disruption of the innate immune cascade could bring about similar results. We crossbred *TAX1BP1*-KO mice with *MyD88*-KO mice [20] and examined the morphological features or immunostaining profiles of marker proteins in the mitral valves of 16-week-old *TAX1BP1*-KO and *MyD88/TAX1BP1*-KO mice. *MyD88/TAX1BP1*-double knockout canceled hyperplasia (Fig. 9A, B), Saa3 induction (Fig. 9C, D) and I-κBα degradation (Fig. 9E, F). Comparisons of ELISA values for *TAX1BP1*-KO and *MyD88/TAX1BP1*-KO mice also indicated amelioration of the inflammatory response in *MyD88/TAX1BP1*-KO mice (Fig. 9G, H).

Discussion

Chronic infection with a retrovirus can have a significant impact on the host immune system. In the case of HTLV-1 infection, the pathological features of the disease are influenced by multiple factors. While HIV causes immune deficiency in the host, HTLV-1 causes a wide range of inflammatory symptoms (HAM and HU) and, in some cases, immunosuppressive ATL, a malignant growth of regulatory T-lymphocytes [39,40]. Furthermore, HAD patients frequently display impaired immune response such as an ineffective interferon response in HAM patients [41] and frequent development of dermatitis in ATL patients [42].

Multiple inflammatory symptoms, including cardiac valvulitis, dermatitis, and a hypersensitive response to endotoxins and inflammatory cytokines, were noted in our preclinical model involving *TAX1BP1-KO* mice. More importantly, *TAX1BP1-KO* mice died prematurely because of unknown mechanisms [8]. In this study, we discovered the hyper-induction of multiple inflammation-related genes including *SAA3*, *CHI3L1*, *HP*, *IL1B*, *SPP1/OPN*, and the significant reduction of *TSC22D3/GILZ* in the mitral valves and microenvironment deterioration in a progressive age-dependent manner for *TAX1BP1*-KO mice [43–47], the

significant reduction of *EFCAB2* expression was highly implicated in functional defects of the heart [36].

HTLV-1-transgenic mice develop autoimmune symptom closely related to those observed for rheumatoid arthritis [48] or Sjögren's syndrome [49]. A rat model, infected with the HTLV-1 producing cell line, is known to develop HAM-like myelopathies in seronegative carrier rats [50]. A Tax1-transgenic mouse model, which specifically expresses Tax1 in T-lymphocytes, illustrates the development of aggressive ATL-like lymphoma with continuous invasion of lymphomatous cells into multiple organs such as the skin, liver and spleen [51,52]. Subcutaneous inoculation of HTLV-1 transformed cells into NOG mice also results in ATL-like symptoms [53]. These transgenic/transplant models show symptoms similar to those found in human clinical cases. Furthermore, HTLV-1-driven inflammatory symptoms tend to occur in patients with HAD under normal host immune response conditions, while ATL-like symptoms develop under immunosuppressive conditions [54].

TAX1BP1-KO mice displayed invasive growth of lymphocytes into multiple organs (Fig. 3) and splenic hypertrophy (Fig. 8). We previously observed that transplantation of *TAX1BP1*-KO bone marrow to γ-irradiated normal mice resulted in the same inflammatory responses [8]. These results imply that *TAX1BP1*-KO model may be correlated with inflammatory HAD. The novelty of this system is identification of possible risk factors associated with vascular disease in HTLV-1 carriers [17,18]. Preliminary electrocardiogram experiments using *TAX1BP1*-KO mice showed an abnormal prolongation of PQ intervals and/or atrioventricular conduction defects (Fig. 6I, J), which might cause fatal cardiac failure. Since the PQ interval and atrioventricular conduction highly depend on the functioning of voltage-dependent L-type Ca^{2+} channels, L-type Ca^{2+} channel function may deteriorate in the heart of *TAX1BP1*-KO mice. Of note, *EFCAB2*, a functional partner in the voltage-gated Ca^{2+} channel, was significantly downregulated in the cardiac tissue of *TAX1BP1*-KO mice (Table 4). Further studies are required to elucidate these defects caused in *TAX1BP1*-KO mice.

Intensive antibiotic treatment [24] for *TAX1BP1*-KO mice significantly ameliorated inflammatory symptoms (Fig. 6). *TAX1BP1*-KO mice crossbred with *MyD88*-KO mice showed similar results. Since the intrinsic role of Tax1bp1 is to inhibit unnecessarily activated innate immunity responses [8], a functional deficiency of Tax1bp1 through HTLV-1 infection can lead to similar symptoms in humans; that is, commensal microbiota can cause pseudo-Infective endocarditis symptoms [55]. The extent of the deficiency, however, is much more moderate than that of typical infective endocarditis (IE) [56].

A large population-based epidemiological study revealed that the prevalence of heart valve disease in the entire population of the United States is 2.5% [53]. IE is thought to result from the following sequence of events: (1) the formation of nonbacterial thrombotic endocarditis on the surface of a cardiac valve or elsewhere that endothelial damage occurs; (2) bacteremia; and (3) the adherence of the bacteria in the bloodstream to nonbacterial thrombotic endocarditis and proliferation of bacteria within a vegetation [57]. Viridans group streptococci are a part of normal skin, oral, respiratory, and gastrointestinal tract flora, and are responsible for ≥50% of community-acquired native valve IE cases [58]. Another review reported that 20% of IE cases originated from culture-negative or Enterococci [59]. Each of these epidemiological surveys clearly indicates the importance of prevention and control measures with regard to microbial infection and vegetation. However, it is still not known why IE is developed in limited population and it is not clear whether there are any differences in the frequencies of allelic polymorphisms in the immune response genes for IE patients?

In summary, HTLV-1 induces diverse forms of inflammatory disorders [60,61], which may originate from the functional dysregulation of Tax1bp1. Single-nucleotide polymorphisms (SNPs) in *A20* or *RNF11*, catalytic partners of Tax1bp1, has have linked to many inflammatory diseases [19,62,63]. However, in the case of *TAX1BP1* SNPs, only one study has linked them to the head and neck cancer [64]. The genetic variations in *TAX1BP1* and its partners would provide novel insights on the pathogenic machinery of HADs.

Supporting Information

Figure S1 Validation of genes identified their expression alteration in the mitral valves of TAX1BP1-KO mice. RT-PCR validation of genes identified their expression alteration in the mitral valves of *TAX1BP1*-KO mice, **A**) *CCL2* **B**) *CHI3L1* respectively. Gray bar: *TAX1BP1*-KO, black bar: WT. Mitral valve specimens were prepared as described in Fig. 2A. Primers and probes were as indicated.
(PDF)

Table S1 Age-dependent induction of pro-inflammatory proteins in the sera of *TAX1BP1*-KO mice. Sera from four different weeks of age (3, 8, 16 and 32) of *TAX1BP1* homozygous knockout (Homo-KO), heterozygous knockout (Hetero-KO) or their WT littermates were collected and examined with multiplex ELISA quantitation kit (Bio-Plex Pro™ Mouse Cytokine 23-plex Assay, BioRad). Each value is an average of four different samples.
(PDF)

Acknowledgments

This paper is dedicated for the memories of the late Dr. Kuan-Teh Jeang who passed away on January 27th, 2013.

Author Contributions

Conceived and designed the experiments: HI KO AN. Performed the experiments: SN EI YT YW T. Matsumoto T. Mitsui TY K. Inoue HK AY K. Ito TS HI. Contributed reagents/materials/analysis tools: SY NT KTJ MH MM TK. Wrote the paper: SN KTJ KO AN HI. Conducted bioinformatics: SN YT WF HI.

References

1. Newton K, Dixit VM (2012) Signaling in innate immunity and inflammation. Cold Spring Harb Perspect Biol 4.
2. McCool KW, Miyamoto S (2012) DNA damage-dependent NF-kappaB activation: NEMO turns nuclear signaling inside out. Immunol Rev 246: 311–326.
3. Hayden MS, Ghosh S (2012) NF-kappaB, the first quarter-century: remarkable progress and outstanding questions. Genes Dev 26: 203–234.
4. DiDonato JA, Mercurio F, Karin M (2012) NF-kappaB and the link between inflammation and cancer. Immunol Rev 246: 379–400.
5. Verstrepen L, Verhelst K, van Loo G, Carpentier I, Ley SC, et al. (2010) Expression, biological activities and mechanisms of action of A20 (TNFAIP3). Biochem Pharmacol 80: 2009–2020.
6. Shembade N, Harhaj EW (2012) Regulation of NF-kappaB signaling by the A20 deubiquitinase. Cell Mol Immunol 9: 123–130.
7. De Valck D, Jin DY, Heyninck K, Van de Craen M, Contreras R, et al. (1999) The zinc finger protein A20 interacts with a novel anti-apoptotic protein which is cleaved by specific caspases. Oncogene 18: 4182–4190.
8. Iha H, Peloponese JM, Verstrepen L, Zapart G, Ikeda F, et al. (2008) Inflammatory cardiac valvulitis in TAX1BP1-deficient mice through selective NF-kappaB activation. EMBO J 27: 629–641.